Kahila, Heikki; Wehrfritz, Armin; Kaario, Ossi; Ghaderi Masouleh, Mahdi; Maes, Noud; Somers, Bart; Vuorinen, Ville

Large-Eddy Simulation on the Influence of Injection Pressure in Reacting Spray A

Large-eddy simulation on the influence of injection pressure in reacting Spray A

Heikki Kahila [a,*], Armin Wehrfritz [a], Ossi Kaario [a], Mahdi Ghaderi Masouleh [a], Noud Maes [b], Bart Somers [b], Ville Vuorinen [a]

[a] Department of Mechanical Engineering, Aalto University School of Engineering, Puumiehenkuja 5, Espoo 02150, Finland
[b] Department of Mechanical Engineering, Eindhoven University of Technology, Den Dolech 2, Eindhoven 5612 AZ, The Netherlands

ABSTRACT

The Engine Combustion Network (ECN) Spray A target case corresponds to high-pressure liquid fuel injection in conditions relevant to diesel engines. Following the procedure by Wehrfritz et al. (2016), we utilize large-eddy simulation (LES) and flamelet generated manifold (FGM) methods to carry out an injection pressure sensitivity study for Spray A at 50, 100 and 150 MPa. Comparison with experiments is shown for both non-reacting and reacting conditions. Validation results in non-reacting conditions indicate relatively good agreement between the present LES and experimental data, with some deviation in mixture fraction radial profiles. In reacting conditions, the simulated flame lift-off length (FLOL) increases with injection pressure, deviating from the experiments by 4–14%. Respectively, the ignition delay time (IDT) decreases with increasing injection pressure and it is underpredicted in the simulations by 10–20%. Analysis of the underlying chemistry manifold implies that the observed discrepancies can be explained by the differences between experimental and computational mixing processes.

© 2018 The Authors. Published by Elsevier Inc. on behalf of The Combustion Institute.
This is an open access article under the CC BY-NC-ND license.
(http://creativecommons.org/licenses/by-nc-nd/4.0/)

1. Introduction

Modern compression-ignition engines aim towards fuel lean, low-temperature combustion (LTC) in order to reduce soot and NOx emissions [1]. In direct injection engines, the fuel is supplied into the engine cylinder by a high-pressure injection system. To optimize the system, the nozzle hole size and shape, number of holes, injection timing or the injection pressure can be adjusted. Supplementary to the injection strategy, the ambient temperature, density and oxygen concentration are important, for instance, when reducing emissions by means of exhaust gas recirculation (EGR). Understanding the complex multiscale physics and chemistry of fuel sprays is essential in order to better control and improve the combustion process.

In compression-ignition direct injection engines the fuel droplets atomize and vaporize forming a high-speed gaseous fuel jet. Such a high-speed jet introduces strong shear, producing turbulence and enhancing fuel-oxidizer mixing. Once the temperature of the compression process exceeds the autoignition temperature and sufficient mixing has ensued, local regions with

the most favorable conditions will ignite. The time from the start of injection (SOI) to ignition is referred to as the ignition delay time (IDT). Directly after the ignition, the flame front expands in three dimensions and forms a quasi-stationary diffusion flame. The diffusion flame stabilizes to a specific distance downstream from the injector, commonly referred to as the flame lift-off length (FLOL). It is worth noticing that the FLOL and IDT both depend on the injection parameters and the ambient conditions described in the previous paragraph [2].

Recent advances in computational resources have enabled large-eddy simulations (LES) of spray flames with high resolution and complex chemical schemes for realistic surrogate fuels. However, numerical model validation requires well defined experimental conditions and for spray flames this has been made possible by the Engine Combustion Network (ECN) [3]. The ECN provides an open-access data repository and a forum for international experimental and numerical collaboration. Baseline target conditions with guidelines for the diagnostic/post-processing techniques have been defined by the ECN for different spray cases. In particular, this study is involved with the ECN *n*-dodecane spray combustion case, designated as Spray A with the following target conditions: ambient gas temperature is 900 K, ambient pressure is approximately 6 MPa and the molar oxygen concentration is 15%.

The injection system has a 150 MPa rail pressure with a nominal nozzle hole diameter of 90 μm. Several experimental studies have been carried out for the non-reacting and reacting Spray A case at different ambient conditions and with different injection pressures [3–9].

The experimental results [3–9], regarding the injection pressure variation, indicate a weak sensitivity of liquid penetration on the injection pressure (see also [10]). In contrast, vapor penetration was found to increase with injection pressure due to the increased momentum of the evaporated fuel. In reacting conditions, the IDT was found to be inversely proportional to the injection pressure, whereas the FLOL was noted to be directly proportional to the injection pressure [3,5,6]. Increase in FLOL with higher injection pressures for different surrogate diesel fuels (not Spray A) has also been reported [11,12].

Computational Spray A studies on injection pressure effects have been previously conducted only in the Reynolds-Averaged Navier–Stokes (RANS) framework. Banerjee et al. [13] reported overpredicted ($\sim$20%) IDT and FLOL by RANS and multi-flamelet representative interactive flamelet (RIF) models. Pei et al. [14] applied RANS and the transported probability density function (TPDF) combustion model for the 50, 100 and 150 MPa injection pressures, with numerical results agreeing with the experiments in terms of FLOL but overpredicting the IDT by $\sim$25%. In general, Spray A related RANS studies have been performed with a variety of different combustion models, including the well mixed combustion model, RIF model [15,16] and the TPDF model [14,17].

In the LES context, Spray A has been previously studied with different combustion models. Gong et al. [18,19] applied the chemistry coordinated mapping (CCM), whereas Pei et al. [20] utilized LES and finite rate chemistry at various ambient temperatures and indicated the relevance of ignition kernels as a flame stabilization mechanism. Blomberg et al. [21] applied the conditional moment closure (CMC) methodology in the split injection Spray A case obtaining good agreement with the experiments in terms of IDT and spatial appearance of low-temperature combustion species, including CH_2O. Recently Hakim et al. [22] used the Bayesian inference calibrated 2-step mechanism together with the dynamic thickened flame model to study the real gas effects and turbulence–chemistry interaction (TCI) on the ignition.

When considering accuracy of the combustion model, CMC [21,23], TPDF [14,24] and finite rate chemistry [20] approaches have provided results which agree well with the experiments. In particular, performance of CMC and TPDF in TCI modeling is notable. In contrast to these computationally demanding methods, another modeling avenue is given by flamelet-based methods, where lookup-tables are computed beforehand to reduce computational overhead [25,26]. Previously, flamelet based methods have been applied to spray combustion under engine like conditions, e.g. by Ameen and Abraham [27] in terms of the unsteady flamelet progress variable (UFPV) model, and by Bekdemir et al. [28] and Tillou et al. [29] with the FGM model. Recently, Wehrfritz et al. [30] applied the FGM model in the Spray A case at different ambient oxygen concentrations. These studies show how the tabulation method can capture the ignition and flame characteristics of the complex non-premixed spray combustion process.

In addition to the choice of the combustion model, the underlying chemical mechanism can vastly influence the results. For example, Wehrfritz et al. [30] showed a consistent offset between the mechanism by Ranzi et al. [31] (130 species) and Narayanaswamy et al. [32] (257 species) within the same LES-FGM framework. Pei et al. [20] attributed their IDT overprediction at low ambient temperatures to the lack of accuracy in the chemical mechanism by Luo et al. [33] (103 species). Other examples of mechanisms applied in LES Spray A context are the mechanism

by Som et al. [34] (103 species) in the LES-CCM work by Gong et al. [18] and the mechanism by Yao et al. [35] (54 species) in the recent LES-CMC work by Blomberg et al. [21].

Spray sub-models are also considered as an important aspect in spray combustion simulations. Typically in engine conditions, the fuel spray poses a short liquid core, due to rapid atomization and evaporation. Therefore, the atomization process is modeled by applying a certain initial droplet size distribution, whereas the secondary droplet breakup is taken into account by sub-models [36]. A thorough literature review related to the challenges in Lagrangian–Eulerian coupling is presented in Ref. [37]. As implied by the literature, the LPT-LES has become a major tool for investigating turbulent spray flames, with varying sub-models [17,18,20,38–40].

Based on the previous literature, there are a number of unexplored questions in the combustion physics of spray diffusion flames and particularly in computational modeling of the ECN Spray A. In this study we continue our previous work on the LES-FGM based Spray A research [30] and formulate the objectives as follows:

1. Compare the computational fuel-oxidizer mixing process in non-reacting conditions with the available experimental data for 50, 100 and 150 MPa injection pressures.
2. Compare the computationally obtained IDT and FLOL with the available experimental data for 50, 100 and 150 MPa injection pressures.
3. Study the potential of the present unsteady flamelet based combustion model to reach a level of detail in low-temperature combustion phenomena and flame stabilization mechanisms equivalent to previous literature (see Pei et al. and Skeen et al. [9,20]).
4. Determine how the size of the low-temperature combustion region is affected by the change in injection pressure.
5. Explain the similarities and discrepancies between different injection pressures from a) the LES modeling and b) from the FGM tabulation perspectives.

The paper is organized as follows: The computational theory and numerical details are provided in Section 2. The computational and experimental set-up is described in Section 3. The results of the non-reacting and reacting cases are analyzed in Sections 4.1 and 4.2, respectively. Further analysis of the reacting results is carried out in Sections 4.3–4.8. A summary and conclusions are given in Section 5.

2. Numerical methods

2.1. Gas phase governing equations

The Eulerian gas phase is described by the compressible Navier–Stokes equations. The Favre-filtered LES formulation for the continuity, momentum and energy equations is the following:

$$\frac{\partial \overline{\rho}}{\partial t} + \frac{\partial \overline{\rho}\widetilde{u}_i}{\partial x_i} = \overline{S_\rho}, \tag{1}$$

$$\frac{\partial \overline{\rho}\widetilde{u}_i}{\partial t} + \frac{\partial (\overline{\rho}\widetilde{u}_i\widetilde{u}_j)}{\partial x_j} = \frac{\partial}{\partial x_j}\left(-\overline{p}\delta_{ij} + \overline{\rho}\widetilde{u}_i\widetilde{u}_j - \overline{\rho}\widetilde{u_iu_j} + \overline{\tau}_{ij}\right) + \overline{S_{u,i}}, \tag{2}$$

$$\frac{\partial \overline{\rho}\widetilde{h}_t}{\partial t} + \frac{\partial (\overline{\rho}\widetilde{u}_j\widetilde{h}_t)}{\partial x_j} = \frac{\partial \overline{p}}{\partial t} + \frac{\partial}{\partial x_j}\left(\overline{\rho}\widetilde{u}_j\widetilde{h} - \overline{\rho}\widetilde{u_jh} + \frac{\overline{\lambda}}{\overline{c_p}}\frac{\partial \widetilde{h}}{\partial x_j}\right) + \overline{S_h}, \tag{3}$$

where $\overline{\rho}$, $\widetilde{u}_i$, $\overline{p}$, $\widetilde{h}$, $\overline{\tau}_{ij}$, denote the filtered density, velocity, pressure, absolute enthalpy and viscous stress tensor, respectively. In particular, the overbar denotes an unweighted ensemble average, whereas the tilde ($\sim$) denotes a density-weighted ensemble average. Variables $\overline{c_p}$ and $\overline{\lambda}$ denote the heat capacity and conductivity.

In Eq. (3) the total enthalpy is expressed as a sum of the absolute enthalpy and the specific kinetic energy, that is, $\widetilde{h}_t = \widetilde{h} + \frac{\widetilde{u}_i \widetilde{u}_i}{2}$. The viscous stress tensor is defined as

$$\overline{\tau}_{ij} = \overline{\mu}\left(\frac{\partial \widetilde{u}_i}{\partial x_j} + \frac{\partial \widetilde{u}_j}{\partial x_i} - \frac{2}{3}\frac{\partial \widetilde{u}_k}{\partial x_k}\delta_{ij}\right), \tag{4}$$

where $\overline{\mu}$ is the dynamic viscosity. The source terms $\overline{S_\rho}$, $\overline{S_{u,i}}$ and $\overline{S_h}$ allow the coupling between liquid and gaseous phases, with respect to mass, momentum and energy. In the reacting cases, the species mass fractions $\widetilde{Y}_k$ are not directly coupled to the solver but are obtained from the combustion model, presented in Section 2.5. The mathematical closure for the system of equations is provided by the filtered ideal gas law and the thermal equation of state.

2.2. Discretization of the governing equations

The governing Eqs. (1)–(3) are solved with the finite volume method. The time integration is based on an implicit, three time-level, and second order accurate scheme. The diffusion terms are discretized by 2nd order central schemes while the convection terms require particular attention due to the high non-linearity of the present compressible reacting flow. Similar to the previous study by Wehrfritz et al. [30], the convective fluxes are interpolated by the Gamma scheme (non-linear flux limiter), developed by Jasak et al. [41]. The Gamma scheme requires an input parameter k, which is chosen in order to control and maintain the 2nd order accuracy in space. A low value indicates less dissipative numerical flux computation. In particular, we chose $k = 0.3$ for the momentum equation while $k = 1.0$ is chosen for the scalars. Based on our numerical sensitivity studies, weak sensitivity between $k = 0.1$ and $k = 0.3$ was noted. Thus, for the momentum equation, we choose $k = 0.3$. Pressure–velocity coupling is implemented in terms of the pressure implicit splitting of operators (PISO) method. The present LES-FGM implementation is based on a standard open-source OpenFOAM-2.4.x spray solver [42].

2.3. Subgrid-scale modeling

The unclosed LES subgrid terms in Eqs. (1)–(3) can be modeled explicitly by introducing additional dissipation via an explicit subgrid-scale model. Alternatively, this dissipation can be introduced and implicitly controlled locally by choosing a dissipative numerical scheme for the convection terms. Here, our choice is such an implicit LES (ILES) as implemented via the non-linear flux limiter, described above. Hence, similar to the previous reacting Spray A study by Wehrfritz et al. [30], we use ILES as a "stand-alone" turbulence model without an any explicit subgrid-scale viscosity. Theoretical work on the similarity between the implicit and explicit SGS models has been carried out in Refs. [43–45]. Previously, the ILES approach has been applied to free shear flows [46,47], supersonic jets [48,49], supersonic combustion [50] and non-reacting and reacting sprays [30,51].

2.4. Spray modeling

Commonly the Lagrangian particle tracking (LPT) method is applied in the modeling of the liquid phase of discrete particles. As a standard practice for the high-velocity sprays, no primary breakup model was used. Instead, the primary breakup is considered by sampling the computational parcels from the Rosin-Rammler size distribution with parameters that lead to the initial Sauter mean diameter of 6 μm.

Equations of motion of the discrete computational parcels can be found from work by Wehrfritz et al. [51], in which the breakup model sensitivity tests for the non-reacting Spray A case were carried out. The results indicated similar global mixture formation

after the liquid phase for the enhanced Taylor analogy (ETAB) and Kelvin–Helmholtz Rayleigh–Taylor (KHRT) breakup models. In the present work, the secondary breakup is modeled by the KHRT model [52,53]. Heat and mass transfer between two phases is modeled according to the standard correlations by Frössling [54], Ranz and Marshall [55,56]. Further details of the spray modeling aspects, along with a mesh sensitivity analysis, can be found from our previous research for the non-reacting Spray A case [51]. A thorough literature review related to the challenges in Lagrangian-Eulerian coupling is presented in [36,37].

2.5. Combustion modeling: the flamelet generated manifold method

2.5.1. Governing equations

The FGM method is based on the theoretical formulation of the intrinsic low-dimensional manifold method (ILDM) [57] and relies on the assumption that a high-dimensional state space of chemical species can be largely recovered by a suitable low-dimensional manifold. In practice, the low-dimensional manifold is represented by the FGM database (a look-up table), which is created in the pre-processing stage from laminar flamelet solutions.

In non-premixed problems mixing must be inherently taken into account, and therefore a one-dimensional laminar counterflow diffusion (CD) flame configuration is often chosen as a canonical case for the flamelet calculations. In the counterflow configuration, the laminar flamelet equations can be expressed as a function of a spatial coordinate x and time t only, and the flow-field effects beyond 1D formulation are included by the local stretch rate $K = \frac{\partial v}{\partial y}$ [58,59]. The one-dimensional conservation equations for the unsteady CD flames can be written as

$$\frac{\partial \rho}{\partial t} + \frac{\partial \rho u}{\partial x} = -\rho K, \tag{5}$$

$$\frac{\partial \rho Y_i}{\partial t} + \frac{\partial \rho u Y_i}{\partial x} - \frac{\partial}{\partial x}\left(\frac{\lambda}{c_p}\frac{\partial Y_i}{\partial x}\right) = \dot{\omega}_i - \rho K Y_i, \tag{6}$$

$$\frac{\partial \rho h}{\partial t} + \frac{\partial \rho u h}{\partial x} - \frac{\partial}{\partial x}\left(\frac{\lambda}{c_p}\frac{\partial h}{\partial x}\right) = -\rho K h, \tag{7}$$

where the variables correspond to definitions in Eqs. (1)–(3) and additionally, $\dot{\omega}_i$ is the chemical source-term of the i-th species Y_i. The local stretch rate K is governed by [60]

$$\frac{\partial \rho K}{\partial t} + \frac{\partial \rho u K}{\partial x} - \frac{\partial}{\partial x}\left(\mu\frac{\partial K}{\partial x}\right) = \rho_{ox}a^2 - 2\rho K^2, \tag{8}$$

where a is the applied strain rate, defined at the oxidizer (ox) boundary. The fuel (at $x = -L$) and the oxidizer (at $x = L$) composition are chosen to correspond to the Spray A conditions.

2.5.2. Manifold parametrization

The manifold parametrization is explained in detail in our previous study [30] but for completeness we outline the essential features here. The solution of the laminar flamelet Eqs. (5)–(8) in the counterflow diffusion flame configuration is computed in physical space and time with the Chem1D code [61]. The solution is obtained with the full chemical mechanism by Ranzi et al. [31] (130 species and 2395 reactions). The mechanism has been shown to predict the ignition delay times and formation of the early reaction products correctly in our previous studies [30,62]. It is assumed that the diffusion of species and heat is dominated by turbulent mixing and therefore a unity Lewis number is assumed for all species.

In order to fill the low-dimensional manifold, a series of steady-state counterflow diffusion flamelets is computed for varying strain rates $a = [1, \ldots, 500]\,\mathrm{s}^{-1}$. Additionally, one unsteady flamelet with the strain rate of 500 s^{-1} is computed to describe

the temporal evolution of the system from ignition towards the steady state solutions on the manifold. It is worth noting that for the same flamelet setup as here, the IDT of the unsteady flamelet has been shown to be quite insensitive to the strain rate when $a < 1000\,\text{s}^{-1}$ [30].

The series of flamelet solutions mentioned above is used to create the 2D manifold, characterized by two control variables. Typical for non-premixed combustion models, these control variables are denoted by the mixture fraction Z and reaction progress variable $\mathcal{Y}$, such that any thermo-chemical quantity ψ from the flamelet solution can be expressed as

$$\psi = \psi(Z, \mathcal{Y}). \tag{9}$$

Mixture fraction describes the essential mixing process of the fuel and the oxidizer in the non-premixed configurations and its definition here is based on coupling functions of element mass fractions using Bilger's weight factors [63,64]. The progress variable is designed so that it can capture the ignition and the reaction progress of the diffusion flame in a monotonic way. The reaction progress variable is defined by a linear combination of reaction products

$$\mathcal{Y} = \frac{Y_{CO_2}}{M_{CO_2}} + \frac{Y_{CO}}{M_{CO}} + \frac{Y_{CH_2O}}{M_{CH_2O}}, \tag{10}$$

where M_k denotes the molecular weight of species k. The present progress variable definition is chosen to represent the first onset of ignition via CH_2O contribution and to progress towards the steady flame via CO and CO_2. The monotonicity of the progress variable is ensured when constructing the manifold, leading to a consistent FGM database.

2.5.3. Subgrid chemistry

During the CFD solution algorithm, only transport equations for the mixture fraction and progress variable are solved, and the thermochemical quantities at the prescribed state can be recovered from the database tables via an interpolation procedure at run-time or later in the post-processing stage according to Eq. (9). When applying the FGM method in the LES context, the Favre-filtered formulation of the appearing FGM-related variable is defined as follows

$$\widetilde{\psi} = \int_0^1 \int_0^1 \psi(Z, \mathcal{C}) P(Z, \mathcal{C}) d\mathcal{C} dZ, \tag{11}$$

where $\mathcal{C} \in [0, 1]$ is the normalized progress variable, defined as

$$\mathcal{C} = \frac{\mathcal{Y} - \mathcal{Y}_{min}(Z)}{\mathcal{Y}_{max}(Z) - \mathcal{Y}_{min}(Z)}, \tag{12}$$

and $P(Z, \mathcal{Y})$ represents the joint Favre-PDF, which is not known a priori. However, here we adopt a widely used approach, based on the presumed joint PDFs for mixture fraction and normalized reaction progress variable

$$\widetilde{\psi} = \int_0^1 \int_0^1 \psi(Z, \mathcal{C}) \beta(Z; \widetilde{Z}, \widetilde{Z''^2}) \delta(\widetilde{\mathcal{C}} - \mathcal{C}) d\mathcal{C} dZ, \tag{13}$$

where the presumed beta and delta-functions are used to approximate the mixture fraction and progress variable subgrid distributions, respectively [25,65–67].

This simplification requires an assumption of statistical independence between the mixture fraction and the normalized progress variable, supported by numerical and experimental results in Ref. [68]. However, in general, the assumption is questionable due to highly non-linear chemical kinetics and a demonstration where this assumption becomes invalid is shown in Ref. [69]. The assumption is rationalized only by its simplicity and is therefore often applied in flamelet based methods, including the current FGM framework.

The mean values of mixture fraction and progress variable in Eq. (13) are obtained from their respective transport equations

$$\frac{\partial (\overline{\rho}\widetilde{Z})}{\partial t} + \frac{\partial (\overline{\rho}\widetilde{u_i}\widetilde{Z})}{\partial x_i} = \frac{\partial}{\partial x_i} \left(\overline{\rho \widetilde{u_i Z}} - \overline{\rho}\widetilde{u_i}\widetilde{Z} + \overline{\rho}\widetilde{D}\frac{\partial \widetilde{Z}}{\partial x_i} \right) + \overline{S_\rho}, \tag{14}$$

$$\frac{\partial (\overline{\rho}\widetilde{\mathcal{y}})}{\partial t} + \frac{\partial (\overline{\rho}\widetilde{u_i}\widetilde{\mathcal{y}})}{\partial x_i} = \frac{\partial}{\partial x_i} \left(\overline{\rho \widetilde{u_i \mathcal{y}}} - \overline{\rho}\widetilde{u_i}\widetilde{\mathcal{y}} + \overline{\rho}\widetilde{D}\frac{\partial \widetilde{\mathcal{y}}}{\partial x_i} \right) + \overline{\dot{\omega}_y}, \tag{15}$$

where $\widetilde{D}$ is the filtered diffusion coefficient satisfying the unity Lewis number assumption and the chemical source term $\overline{\dot{\omega}_y}$ is obtained from the FGM database according to Eq. (13). The subgrid mixture fraction variance in Eq. (13) is estimated using an algebraic model [70] $\widetilde{Z''^2} = C_v \Delta^2 |\frac{\partial \widetilde{Z}}{\partial x_j}|^2$, where C_v is a dynamically evaluated model coefficient [71] and Δ denotes the LES filter width (cell size). The unclosed subgrid-scale terms in Eqs. (14) and (15) are again modeled implicitly by applying the ILES methodology, which was discussed in Section 2.3.

2.5.4. Manifold construction and coupling to the LES solver

The FGM database has $141 \times 161 \times 21$ data points for mixture fraction, progress variable and mixture fraction variance, respectively. The data points are clustered close to the stoichiometric mixture fraction and refined towards the lower progress variable values. Similarly higher resolution for low mixture fraction variance values is used.

The most important tabulated variable is the progress variable source term $\overline{\dot{\omega}_y}$, which appears explicitly in the transport Eq. (15). However, additional variables are included in the database, to do run-time post-processing and to achieve consistent thermodynamics for the two-phase spray configuration. The LES spray solver is implemented in terms of absolute enthalpy and the corresponding temperature is computed utilizing the mixture averaged heat capacity, which allows accounting for cooling effects due to droplet evaporation. Therefore, a representative set of species mass fractions (15 out of 130) is included in the FGM database to represent the mixture composition in the LES. Importantly, no transport equations for these species are solved, but they are purely taken from the FGM database. However, this subset of species does not conserve mass, energy or thermodynamic properties of the realistic mixture at all stages of combustion. Therefore, a constrained sequential least squares programming procedure is applied for the representative species to modify their properties such that conservation is achieved. A more detailed explanation of the optimization procedure can be found from our previous work [30]. It is noteworthy that species included in important post-processing utilities, e.g. fuel, OH and CH_2O are not part of the optimization procedure.

3. Spray A configuration

3.1. Computational set-up

The discretized domain corresponds volumetrically to the experimental combustion vessel at the Sandia National Laboratories [3] and consists of 11.5 million hexahedral cells. The smallest cells, with a size of 62.5 μm, cover the space between the nozzle and 35 mm downstream, to ensure sufficient resolution in the location where the ignition and flame stabilization takes place. The rest of the vapor penetration region and the region where combustion mainly takes place are discretized with 125 mm cells. It has been concluded in studies by Xue et al. [40], Pei et al. [20] and Wehrfritz et al. [51], that a cell size of at least 62.5 mm is needed for good quality LES in sprays. The time step in all cases was set to 40 ns, resulting in a maximum Courant number of 0.33.

The same initial droplet size distribution and breakup parameters were applied for all three injection pressures due to lack of

Table 1
The Spray A specifications.

Injection conditions	
Fuel	n-dodecane (n-$C_{12}H_{26}$)
Nominal nozzle diameter, D	90 μm
Fuel temperature	363 K
Injection pressure	50,100, 150 MPa
Ambient conditions	
Ambient temperature	900 K
Ambient density	22.8 kg/m³
Ambient O_2 % (molar)	0 and 15

a priori information on the explicit dependence of the parameters on the injection pressure. The injection profile was adopted from a virtual profile generator [72], as suggested by the ECN. The ambient conditions, fuel injection specifics and experimental results are based on the ECN guidelines [3] and presented in the following section. It is worth noting that the simulation end time for the non-reacting cases was set to 2 ms, whereas for the reacting cases it was set to 1.5 ms.

3.2. Experimental Spray A conditions

The present computations are carried out for the experimental ECN Spray A baseline conditions as defined in Table 1 [3]. Liquid n-dodecane is injected from a 90-μm diameter nozzle hole into the combustion vessel, with an ambient gas composition of O_2, N_2, CO_2 and H_2O in thermodynamic conditions given in Table 1. In reacting studies, the molar fraction of oxygen is set to 15% and other scalars with respect to the corresponding condition [3]. Injection pressure is the only varying baseline parameter in the present study.

The numerical LES results are compared to experimental data originating from Sandia, TU/e or CMT, depending on the available data for the specific quantity. The baseline conditions are the same in each experimental configuration. Distinctively, the experiment takes place in either a constant volume combustion vessel (Sandia, TU/e) or a constant flow combustion vessel (CMT).

4. Results and discussion

4.1. Non-reacting evaporating spray results

Following a validation procedure similar to various previous Spray A studies [14,18,30], we first investigate the spray in non-reacting, evaporating conditions [3]. The monitored quantities are 1) vapor penetration, 2) liquid penetration, and 3) average radial mixture fraction profiles. The liquid and vapor penetrations, as specified by the ECN, are defined as the farthest axial distance with 0.1% liquid volume and gaseous fuel mass fraction.

Figure 1 shows the liquid and vapor penetrations for the three injection pressures with the comparison to the experimental data. The computed vapor penetration profiles are within the experimental error margin at the early stage of injection ($t < 0.5\,\mathrm{ms}$) and start to deviate only slightly at later times. Liquid penetration for the 50 MPa case is slightly underpredicted and oscillates more compared to the higher injection pressures.

The effect of injection pressure is clearly visible from the vapor penetration curves: a higher injection pressure accelerates the liquid phase to a higher velocity and therefore induces higher gas velocity and turbulence levels. Mixing is enhanced and the vaporized fuel has more momentum to penetrate farther into the domain. In contrast, the sensitivity of the liquid penetration to the injection pressure is small. Such insensitivity of liquid penetration
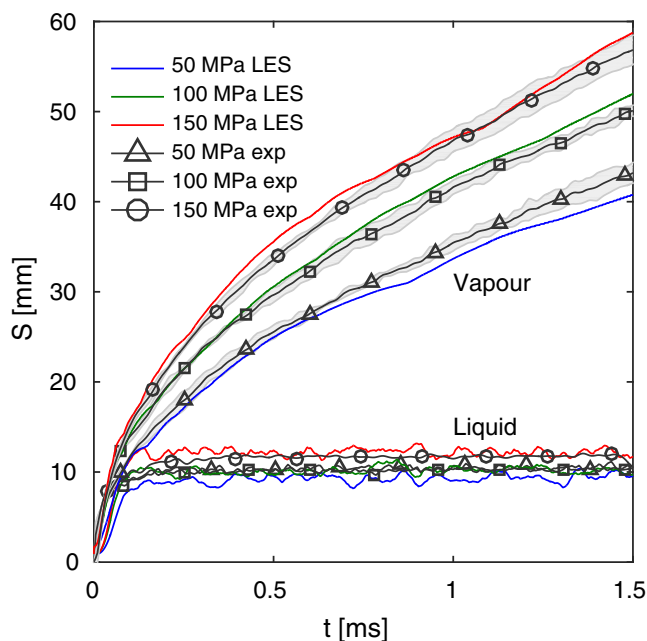

Fig. 1. Liquid and vapor penetration at the injection pressure range for simulated (solid lines) and experimental [3,73] (symbols) cases. The filled area is the corresponding experimental standard deviation.

to injection pressure has been previously experimentally recognized and designated as "mixing limited" vaporization: injection pressure dependent change in mass flow rate is compensated by the change in overall evaporation rate, which is controlled by the air-entrainment [10,38].

Figure 2 shows the mean radial mixture fraction profiles at three axial locations. The profiles are obtained from a single LES realization by azimuthal and time averaging the data. The azimuthal averaging is carried out around the spray axis by dividing the domain into $N_\phi = 90$ planes. The plane data is furthermore averaged between 1.5 and 2 ms in time. In Fig. 2, the shaded area around the mean profiles corresponds to the standard deviation of the mixture fraction. It is noteworthy that the azimuthal space averaging is fully correlated at $r = 0$ so therefore the standard deviation near the spray axis is only due to temporal variations.

The mean profiles for all injection pressures agree well with the experimental data at $z = 17.9$ mm, i.e. the first upstream location where experimental data is available. This location is interesting when later considering the FLOL values, which e.g. for the 150 MPa case is 17.4 mm. However, further downstream from the nozzle the profiles are underpredicted and the 50 MPa case experiences highest deviations close to the spray axis. The agreement between the simulated and experimental mean profiles is slightly enhanced when $z > 30$ mm.

Acknowledging the general view that the LPT submodels can influence spray results to great extent, we decided to further investigate the sensitivity of the ILES approach on the non-reacting spray results while keeping the LPT submodels fixed. As in the previous study by Wehrfritz et al. [30], numerical dissipation of the ILES approach is produced by a 2nd order accurate flux limiting scheme [41], with the pre-specified constant k allowing control of the local numerical dissipation. We examined three different values: $k = 0.1$, $k = 0.3$ and $k = 1.0$, corresponding to the non-dissipative and dissipative behavior, respectively. The effect of k at two extremes was clear: with $k = 1.0$ the momentum of the vapor jet appeared more centered on the spray axis and air-entrainment was reduced, resulting in very high mixture fraction values near the spray center, compared to the lower coefficient value. However, the results
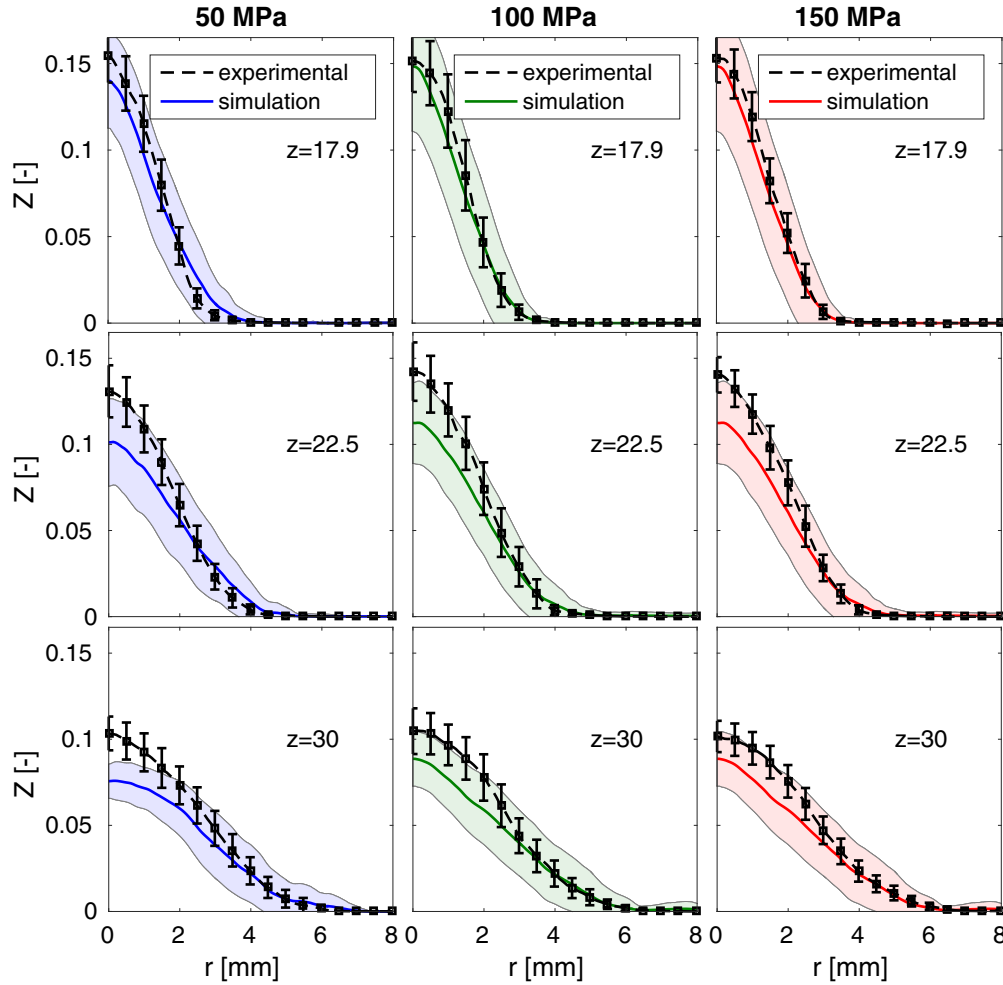
Fig. 2. Mean mixture fraction radial profiles (solid lines), computational standard deviation (filled area) and experimental 95% confidence interval (error bars). Experimental data is obtained from Rayleigh-scattering imaging [3,73]. Axial locations are: top row $z = 17.9$ mm, mid row $z = 22.5$ mm and bottom row $z = 30$ mm.

indicated only small difference between $k = 0.1$ and $k = 0.3$ and therefore the value $k = 0.3$ was applied in the final simulations.

The presented validation procedure shows that the present LES-LPT combination reproduces the non-reacting Spray A characteristics with an accuracy level comparable to the previous LES studies [17,19,40]. In particular, the results indicate that the chosen ILES approach and LPT submodels together are capable of reproducing the experimentally observed trends on Spray A development. However, the underprediction of the radial profiles is expected to affect, to some extent, the nature of the modeled diffusion flame.

4.2. Global view of ignition and flame lift-off

As mentioned, the present LES-FGM study is a follow-up study for the previous work by Wehrfritz et al. [30] where varying ambient oxygen concentrations were investigated. However, the ability of the same model to capture the IDT and FLOL with varying injection pressures is an open question. Figure 3 shows the temperature field evolution in time for the three cases, illustrating a typical two-stage ignition characteristic for n-dodecane. At an early stage of injection ($t = 0.25$ ms, first row), the fuel vapor jet has not yet experienced extensive turbulent mixing and there is no global sign of ignition. At $t = 0.35$ ms (second row) the cold fuel vapor experiences relatively strong mixing with the hot ambient air, leading to an early chemical heat release in the fuel-rich part of the spray. The vapor temperature increases in such parts by 200–300 K, resulting from the so-called first-stage ignition.

The second-stage ignition is observed in the low velocity stagnation region close to the tip of the vapor jet, which is clearly seen for all the cases from the first occurrence of high temperatures at $t = 0.45$ ms (row 3) in Fig. 3. At the beginning of the second-stage ignition, multiple igniting gas pockets, i.e. ignition kernels, are formed almost simultaneously in the vicinity of the jet tip. Such a process resembles a volumetric ignition phenomenon depicted in previous experimental and numerical studies [9,20,39,74,75]. After the second-stage ignition, a high-temperature diffusion flame expands in three dimensions and stabilizes with an injection pressure dependent distance downstream from the injector, i.e. at the FLOL.

Figure 4 shows a quantitative comparison of the simulated and measured IDTs and FLOLs as a function of the injection pressure. The IDT is defined according to the ECN guidelines as the first time at which the instantaneous OH mass fraction reaches 2% of the maximum in the domain after a stable flame is established. The inverse proportionality of the IDT to the injection pressure is captured but the slope and the experimental values are underestimated with a maximum deviation of $\sim 20\%$. Qualitatively, the present results are consistent with the previous observations by Wehrfritz et al. [30].

Figure 5 shows the time evolution of the mean pressure rise in the combustion chamber. At early times after SOI, a modest pressure decrease is observed due to the cooling effects of the liquid evaporation. After the second stage ignition, pressure rises rapidly: the higher the injection pressure, the higher the rate of
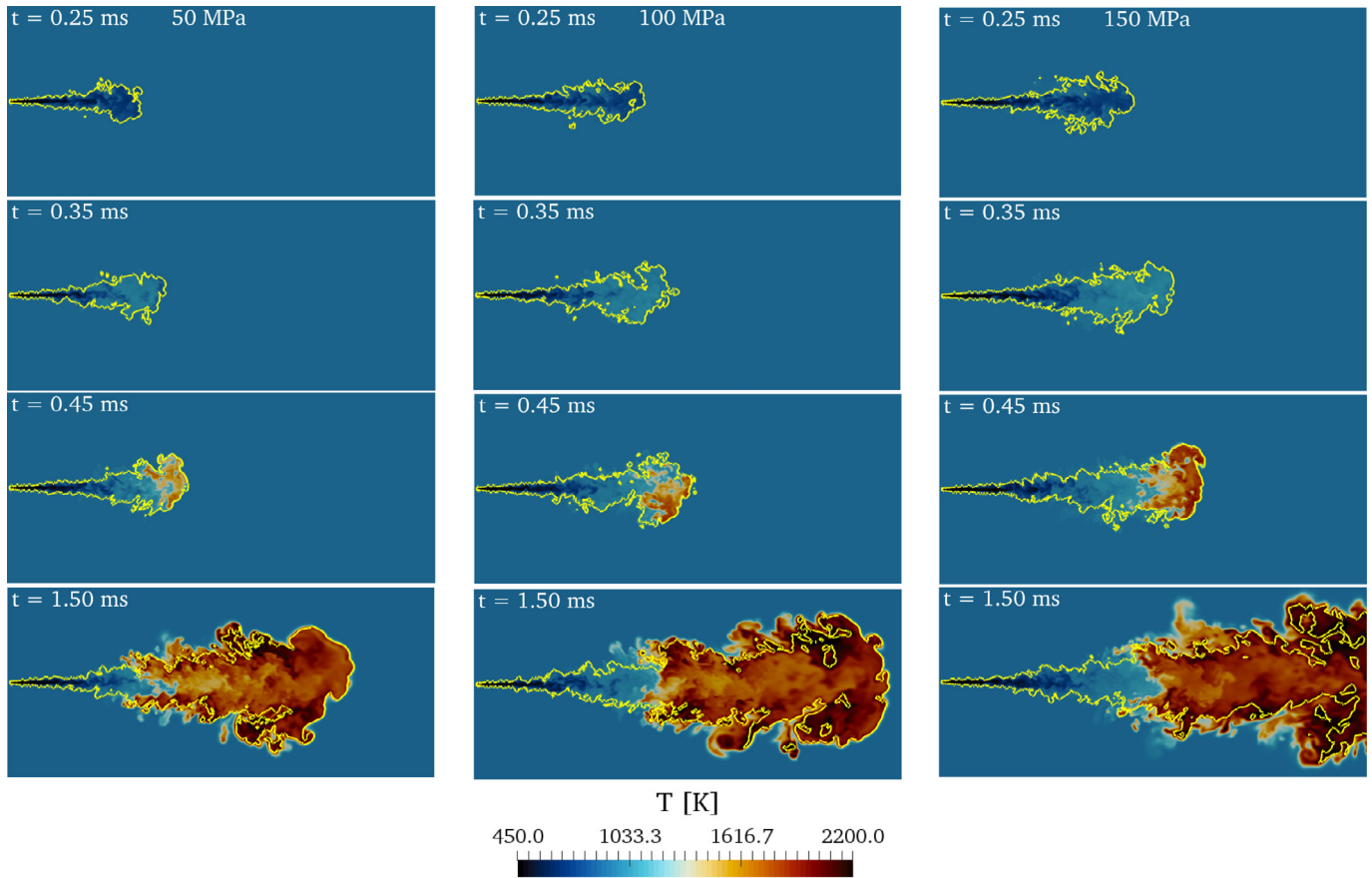
Fig. 3. Instantaneous temperature fields. Left column 50 MPa, mid column 100 MPa and right column I150 MPa. From top to down: 0.25, 0.35, 0.45 and 1.5 ms in time. The stoichiometric mixture fraction Z_{st} is shown as a yellow contour line. (For interpretation of the references to color in this figure legend, the reader is referred to the web version of this article).
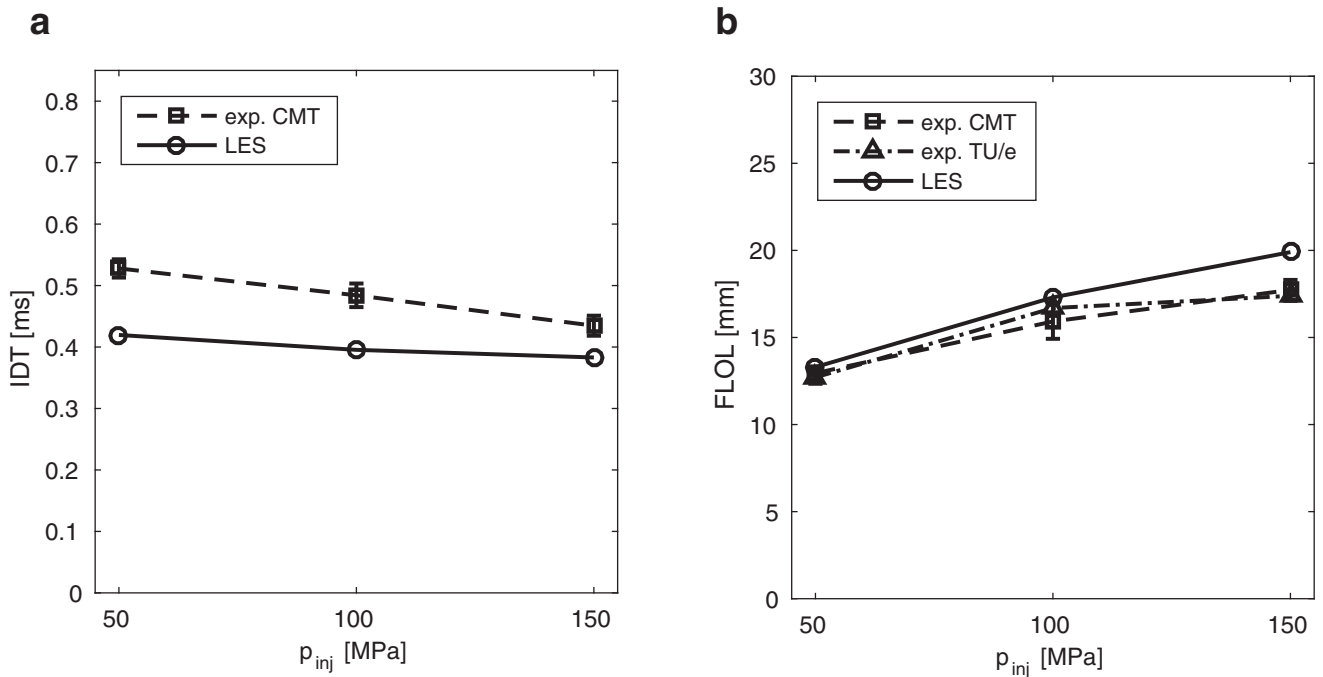
Fig. 4. (a) Ignition delay time and (b) flame lift-off length as a function of injection pressure. Experimental results are from CMT [5] and TU/e [6]. The error bars indicate the standard deviation.
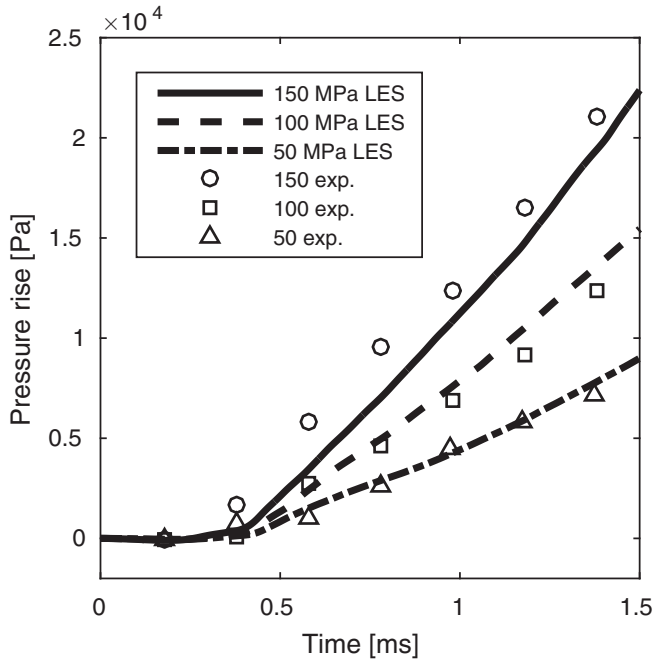
Fig. 5. Time evolution of the pressure rise in the combustion chamber. Lines represent numerical and symbols experimental results [6].

pressure rise which is consistent with the increased mass flow rate. The slopes of the pressure rise are captured well with the current LES-FGM configuration and can be interpreted as a result of comparable global mixing processes between LES and experiments. Importantly, when considering the absolute experimental values of the IDTs between Figs. 4a and 5, there seems to be an inconsistent trend between the injection pressures. As the pressure rise indicates, the 50 MPa case experiences the first minor pressure rise earlier than the 100 MPa case. This can be attributed to the temporal data-acquisition uncertainties in the pressure rise experiments [6]. Furthermore, the luminosity based IDT definition in Fig. 4a, is expected to yield higher IDT values compared to the respective early pressure rise definition.

After the second-stage ignition, the spray diffusion flame stabilizes at a downstream position referred to as the flame lift-off length (FLOL). This can be seen on the last row of Fig. 3. Quantitatively, FLOL is defined according to the ECN guidelines as the first axial location of the Favre-averaged OH mass fraction reaching 2% of its maximum in the domain. The averaging was carried out azimuthally in space and between 1.4 and 1.5 ms in time. The numerical FLOL values are compared to the experiments in Fig. 4b with good agreement, even though a slight overprediction can be observed. The deviation between the experimental and numerical FLOL varies between approximately 4–14% in the considered injection pressure range. Further analysis on the noted discrepancies in IDT and FLOL will be discussed in Sections 4.5–4.7.

Typically in experiments, the FLOL is determined from the excited state of OH (OH*) but in numerical studies the aforementioned 2% OH_{max} standard is often applied. Therefore, it is also interesting to see how the overall hydroxyl (OH) field is captured by the numerical model. Recently, Maes et al. [6] carried out experiments of various Spray A conditions, including an injection pressure variation, using chemiluminescence and single-shot planar laser-induced fluorescence (PLIF) of OH (not the excited state). A detailed description of the optical diagnostic techniques is given in Ref. [6] and is only briefly outlined in the following. A frequency-doubled dye laser was operated on Rhodamine 6G in order to excite the ground state hydroxyl radical at a wavelength
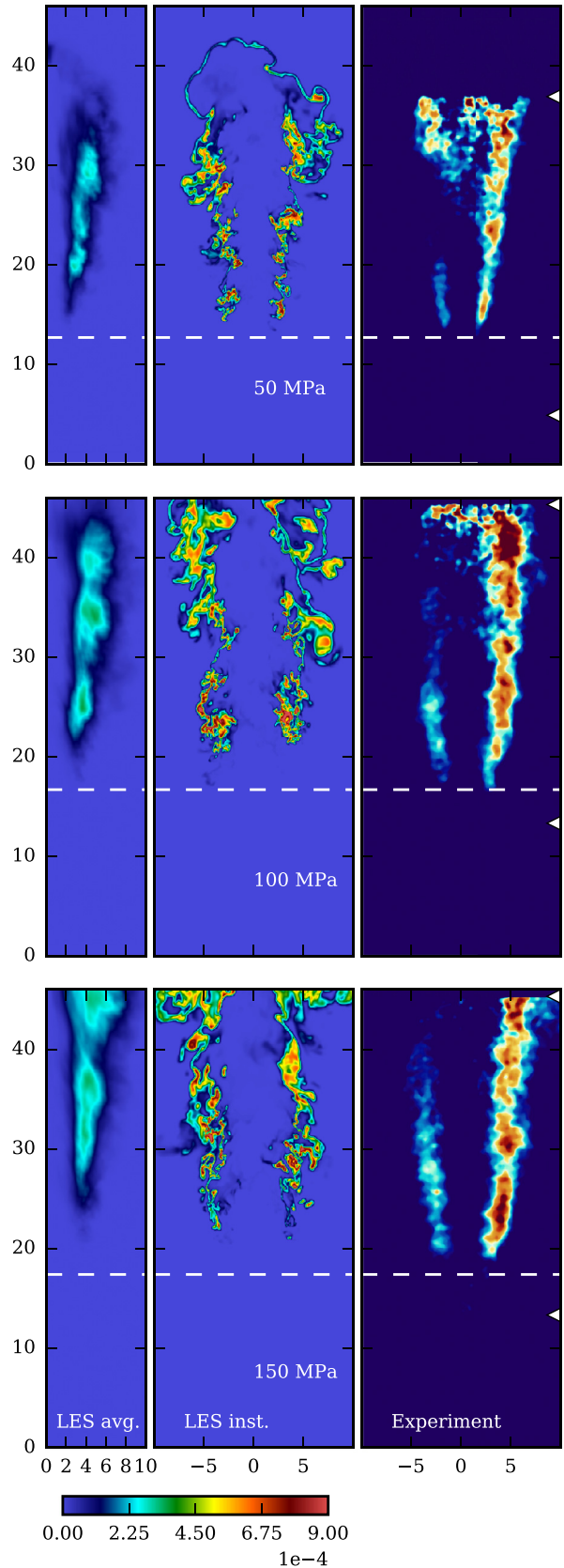

Fig. 6. Spatial OH distributions for the three injection pressures. The two figures on the left show an averaged (in space and time) and instantaneous snapshots at time $t = 1.5$ ms from the LES. The experimental PLIF data from Maes et al. [6] is shown on the right. Units are in millimeters. The dashed vertical line indicates the experimental FLOL based on OH* chemiluminescence measurements. The white triangles on the right side mark the laser sheet location.

of 283.93 nm and 11 mj/pulse. The output was used to form a 30-mm wide sheet at the location of the spray. An intensified CCD camera was placed such that only the illuminated region was captured (the injector was located outside the field-of-view), in order to increase signal detection. For each injection pressure variation, 10 or more PLIF recordings were obtained to generate an ensemble-averaged image at a time of 4.7 ms after SOI.

Figure 6 shows a qualitative comparison of the OH distribution obtained from the LES and PLIF experiments for the three injection pressure cases. The results from the PLIF experiments are shown in the right and the averaged and instantaneous LES fields in the two left-most columns, respectively. The averaging for the LES results was carried out azimuthally in space and between 1.4 and 1.5 ms in time. No additional filtering or post-processing of the LES result is applied due to qualitative nature of the comparison. It should be noted that the reduced PLIF signal intensity in the left OH branch can be attributed to the attenuation of excitation laser light by the central regions of the spray (PAH and soot) [76,77]. Absence of a left OH branch upstream of locations, where signal appears in the central part of the spray, indicates that the detected intensity arises from incandescence, rather than from fluorescence.

The spatial location and shape of OH predicted by the LES agrees reasonably with the experimental PLIF data for all three injection pressures. For the higher injection pressure cases, the onset of OH formation is located farther downstream than in the corresponding experiments, being consistent with the deviations noted in Fig. 4b. The experimental results indicate that the intensity of hydroxyl is expected to reach relatively high values already near the FLOL region, whereas the LES results indicate a faint decrease of OH closer to FLOL region.

4.3. Ignition in mixture fraction space

The results above indicate that the observed trends for the FLOL and IDT are reasonably well predicted by the present model. Next, we further explore the ignition characteristics in the mixture fraction space and show certain similar aspects between all the cases. Figure 7 shows the temporal evolution of the spray in the resolved temperature-mixture fraction plane. Scatter points are colored by the mass fraction of formaldehyde and superimposed partially by the mass fraction of hydroxyl. Only data points with $Z > 0.001$ are considered and OH is superimposed only for OH $> 2\%$ OH$_{max}$, enabling a clear visualization. In addition, the expectation value for the conditional temperature with respect to mixture fraction $\langle T|Z \rangle$ is indicated by a red line. It is worth noting that the current scatter plots and the conditioned means are computed from the local resolved scalar data, neglecting the SGS variance contribution.

Figure 7 shows the onset of the first-stage ignition at $t = 0.15$ ms (first row) near the stoichiometric isoline ($Z_{st} = 0.045$), resulting only in a slight increase in temperature (I). Temperature decreases with increasing mixture fraction, following the adiabatic mixing line. The (Z, T) point pairs start to deviate slightly from the adiabatic mixing line at high mixture fraction values due to evaporative heat loses. The second row shows the propagation of the mean heat release towards richer conditions (II) at $t = 0.3$ ms. Further, at $t = 0.4$ ms, the mean temperature is starting to peak around $Z \approx 0.12$ (III, row 3).

The OH concentration is significantly increased between 0.4 and 0.45 ms near the stoichiometric conditions in Fig. 7 (IV). This stage corresponds to the high temperature ignition kernels in the vortices at the tip of the vapor jet, shown by the temperature fields in Fig. 3. It has been proposed that the formation of OH radicals results from the reaction chains, induced by the auto-ignition on the fuel-rich side [78]. Next, combustion develops rather quickly in ZT-plane towards higher temperatures and leaner conditions (V), being inline with previous studies [18,20,79,80].

Table 2

Summary of the presented results. Experimental results inside the brackets (Liq. Pen.: [3,73], IDT: [5], FLOL: [6]). C$_{FL}$ refers to the cool flame length.

	Liq. pen [mm]	IDT [ms]	FLOL [mm]	C$_{FL}$ [mm]
50 MPa	9.3 (10.8)	0.420 (0.528)	13.3 (12.71)	17.3
100 MPa	10.1 (10.5)	0.395 (0.484)	17.3 (16.69)	20.4
150 MPa	12.2 (10.0)	0.383 (0.435)	19.9 (17.39)	24.1

Finally a quasi-steady high temperature diffusion flame is formed, which is indicated by the narrow band of OH, peaking at the stoichiometric mixture fraction. Figure 8 shows how the OH field envelopes the high temperature zone in space.

Consistent with several previous studies [18,20,23,78–81], the herein observed late auto-ignition does not take place at the stoichiometric conditions but occurs more on the fuel rich side. This trend can be related to the most reactive mixture fraction (Z_{MR}) concept [78] which describes how the auto-ignition chemistry may prefer a certain mixture fraction regime different from the stoichiometric conditions. For example, the early reaction products close to the stoichiometric conditions can be transported into rich mixtures, promoting low-temperature reactions therein [79]. Feasibility of the Z_{MR} concept in turbulent non-premixed auto-ignition problems has been further discussed in the recent DNS studies [82–84].

In order to estimate Z_{MR} in the present system, we carried out 0D homogenous reactor computations with initial conditions taken from the mixing line [78]. The composition yielding the shortest IDT with the current chemical mechanism was found to be $Z_{MR} \approx 0.078$. Similarly, Wehrfritz et al. [30] showed how heat release of the transient auto-igniting 1D flamelet begins near the stoichiometric conditions, then subsequently drifts towards rich mixtures ($0.1 < Z < 0.15$), and finally leads to the high-temperature ignition around ($0.06 < Z < 0.1$) consistent with the value $Z_{MR} = 0.078$. The results for the three LES cases presented in Fig. 7 indicate similar ignition characteristics as 1D flamelets, which is expected because of the shared flamelet based chemistry manifold. Recent DNS studies on non-premixed auto-ignition show how the ignition occurs at slightly higher values than Z_{MR} with relatively low scalar dissipation rates [83,84].

Hence, the most reactive mixture fraction concept is useful in understanding ignition in spray LES as well. We note that for the lowest 50MPa injection pressure, the early heat release yields a slightly broader distribution in mixture fraction space while the high-temperature ignition occurs quite similarly for the all cases around ($0.06 < Z < 0.1$).

4.4. Spatial and temporal role of low-temperature combustion

In Fig. 7, the regions withion and elevated mean temperature in the range of $0.1 < Z < 0.15$ mark the formation of a stabilized formaldehyde pool, also called the "cool flame" upstream from the diffusion flame [9,30]. The cool flame and its spatial appearance is presented in Fig. 8 together with the OH field which envelopes the high-temperature zone of the diffusion flame. Next, we consider the fourth objective of this work and investigate the structure and position of the cool flame.

Figure 9 shows the average CH$_2$O mass fraction along the spray axis for the three injection pressures. The profiles indicate a more confined region of formaldehyde when injection pressure decreases. This observation is related to the shortened FLOL and thereby also earlier CH$_2$O consumption. The mean cool flame lengths are estimated based on a threshold of 2% of the maximum formaldehyde mass fraction and the results are gathered in Table 2. As an example, the temporal evolution of formaldehyde concentra-
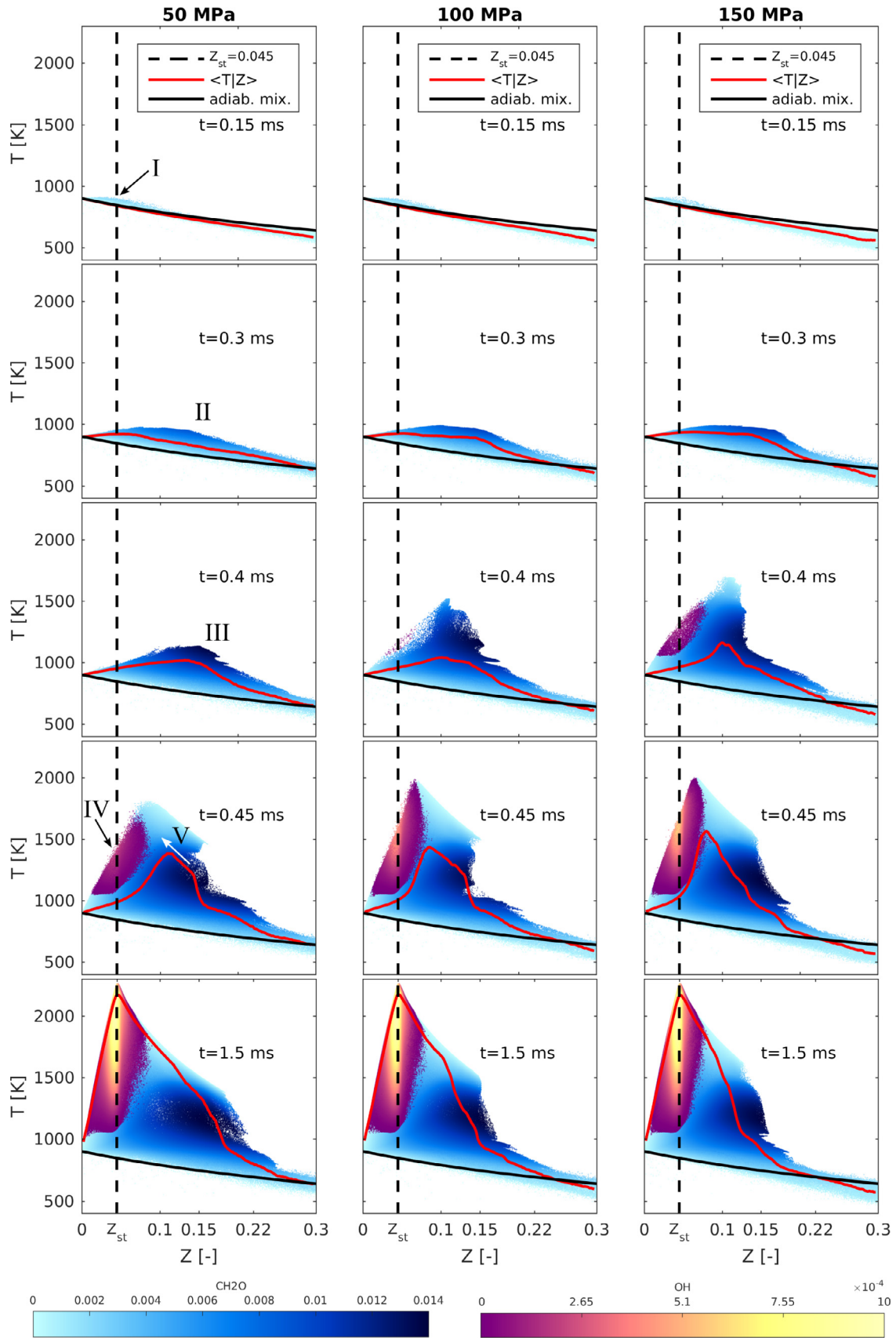
Fig. 7. Scatter point representation in ZT-plane, colored by CH_2O and superimposed by $OH > 2\%$. The red solid line marks the mean temperature conditioned with respect to mixture fraction. The black solid line marks the adiabatic mixing line. (For interpretation of the references to color in this figure legend, the reader is referred to the web version of this article).
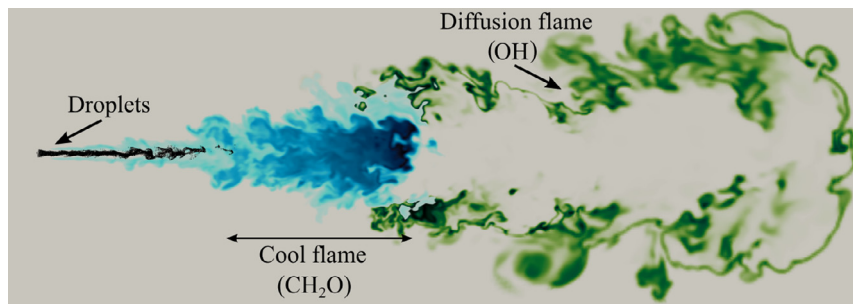
Fig. 8. Spatial CH_2O and OH fields for the 100MPa case at $t = 1.5$ ms.
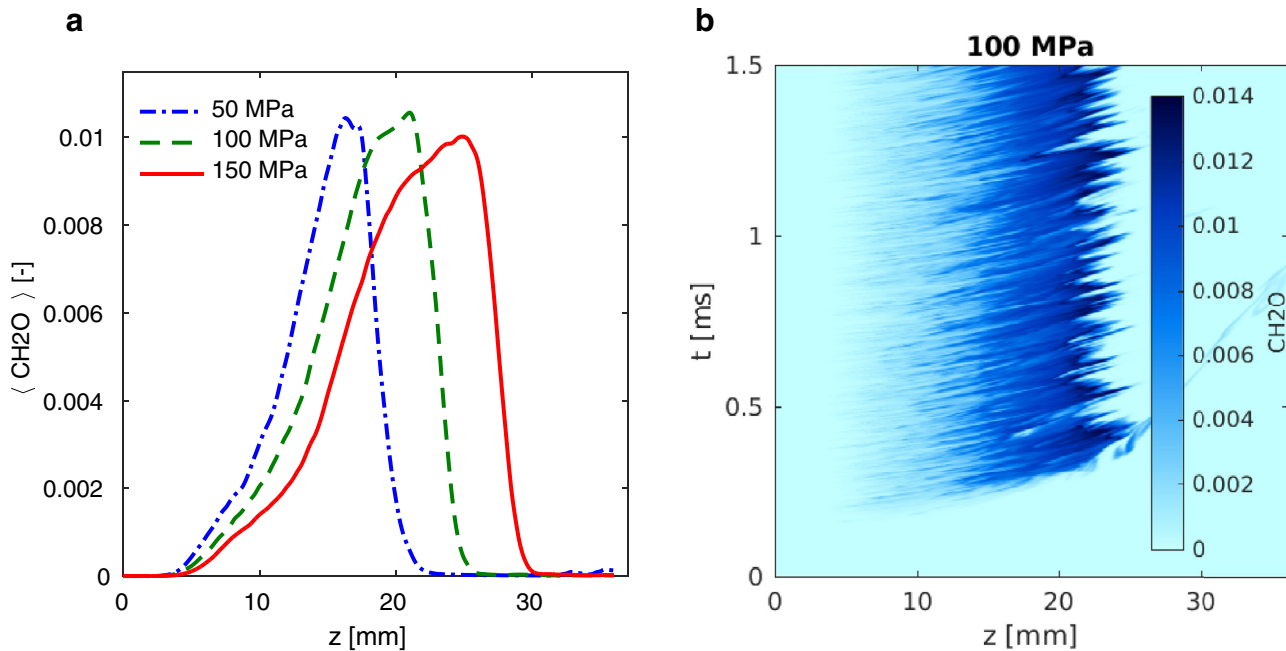

Fig. 9. (a) Averaged formaldehyde mass fraction along the spray axis and (b) time evolution of the formaldehyde mass fraction along the spray axis for the 100 MPa case.

tion on the spray axis is shown in Fig. 9b. It is noted that the cool flame length stabilizes rather quickly, being phenomenologically in line with the experimental observations by Skeen et al. [9].

In addition, an interesting element related to the cool flame can be seen on the last row in Fig. 7. For the 50MPa case, the conditional mean temperature curve shows higher temperature values at rich mixture conditions ($Z > 0.12$), compared to higher injection pressures. This can be understood by considering the temperature fields in Fig. 3 and FLOL behavior in Fig. 4b. A lower injected momentum produces a lower level of turbulent fluctuations and mixing, subsequently yielding a shorter FLOL. As a result, also the cool flame appears closer to the nozzle at richer mixtures, see Fig. 9a. A broader Z-distribution at higher temperatures for low injection pressure is also consistent with experimental observations of increased soot formation with lower injection pressures [11,12]. The main quantitative results and corresponding experimental values from the reacting studies are gathered in Table 2.

### 4.5. Early phases of the volumetric ignition

As already indicated in Fig. 4a, the present LES-FGM model under-predicts the experimental IDT and also poses a weaker sensitivity to the injection pressure. However, Fig. 7 indicates quite similar ignition process between the injection pressures in the ZT-plane. Additionally, the ignition always starts from the spray tip. Next, explanations to the aforementioned IDT off-set and

weak injection pressure sensitivity are further explored from the viewpoint of the present model.

Even though higher injection pressures promote faster mixing of the fuel, the numerical results show clear similarities in the mixing processes for the three injection pressures, see Fig. 7. Motivated by these observations, it is interesting to investigate the similarity of the ignition processes for the three pressures along the spray axis in zt-plane. Figure 10 shows the time evolution of the progress variable along the spray axis for the high and low injection pressures, prior to ignition. The time of the first appearance of the progress variable source term value above $\overline{\dot{\omega}_y} = 1000 \, \text{kg} \, \text{m}^{-3} \text{s}^{-1}$, takes place ca. 0.23 ms before the actual ignition. Finally, a pathway towards the high-temperature ignition begins ca. 0.13 ms before the IDT and is visible in Fig. 10 by the source term isoline of $\overline{\dot{\omega}_y} = 2.5 \times 10^5 \, \text{kg} \, \text{m}^{-3} \text{s}^{-1}$. It is interesting to see such characteristic behavior for both extreme injection pressures. This observation implies that in the present model the ignition delay time is, to some extent, characterized by the time when the first high axial progress variable source term values appear. Thereby, the observed IDT depends not only on chemistry but also on the early mixing process on the resolved scales. Regarding the mixture formation, see also Section 4.3 for discussion on the most reactive mixture fraction.

In order to extend the overview of the early stages of ignition, Fig. 11 shows the evolution of formaldehyde from $t = \text{IDT} - 0.15$ ms to $t = \text{IDT} - 0.1$ ms. Since formaldehyde is
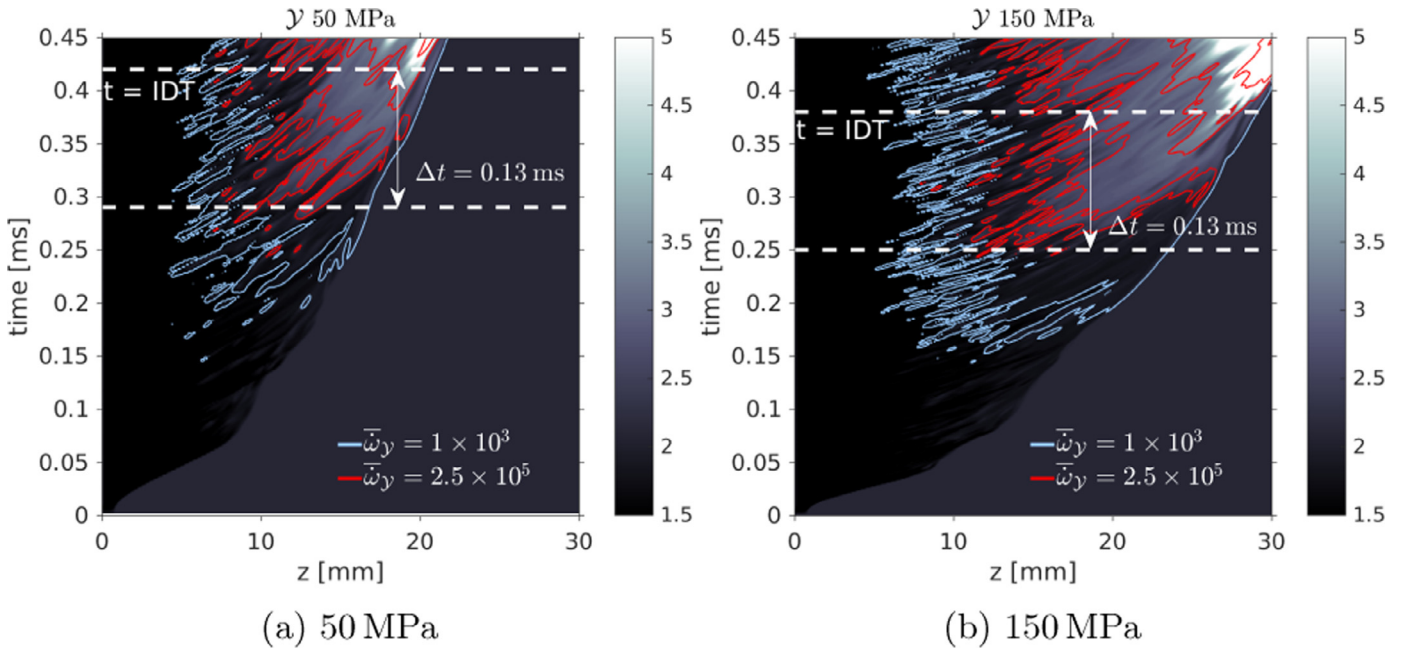
Fig. 10. Time evolution of progress variable $\mathcal{Y}$ on the spray axis for the (a) 50 MPa and (b) 150 MPa cases. The light blue and red contour lines represent the progress variable source term values $\overline{\dot{\omega}}_y = 1000 \, \text{kg} \, \text{m}^{-3} \text{s}^{-1}$ and $\overline{\dot{\omega}}_y = 2.5 \times 10^5 \, \text{kg} \, \text{m}^{-3} \text{s}^{-1}$, respectively. The white solid lines represent the time of ignition and the time 0.13 ms before the ignition. (For interpretation of the references to color in this figure legend, the reader is referred to the web version of this article).

also part of the progress variable, the overall evolution of $\mathcal{Y}$, shown in Fig. 10, is consistent with the following findings. At early times ($t = \text{IDT} - 0.15$ ms and $t = \text{IDT} - 0.13$ ms), small amounts of formaldehyde are formed near the stoichiometric conditions at the sides of the fuel spray, being consistent with the scatter plots in Fig. 7 (I). Progressively, the turbulent mixing and consequent production of $\mathcal{Y}$ leads to a formation of a confined formaldehyde region in the center part of the spray jet. Such a region is visualized by CH_2O in Fig. 11 at $t = \text{IDT} - 0.1$ ms corresponding to higher axial $\mathcal{Y}$ and $\overline{\dot{\omega}}_y$ values in Fig. 10. Similar low-temperature combustion propagation from lean outer regions to the richer core of the spray was recently reported by Dahms et al. [79].

The simulated cases share the same chemistry (same FGM tables) and as Figs. 10 and 11 show, both 50 and 150 MPa cases share also a very similar pathway to the second stage ignition. Apparently, the performed LES is unable to produce characteristically large enough differences to the scalar field formation and transport which is important to the functionality of the FGM model and therefore to the observed IDT values. There are various numerical modeling aspects which could potentially influence the presented results, including multiphase momentum transfer, droplet breakup and evaporation models, numerical diffusion, ILES subgrid-scale model and mesh resolution. Additionally, the present FGM implementation applies only one flamelet solution with a strain rate of $500 \, \text{s}^{-1}$ to construct the igniting part of the manifold. The scalar dissipation rate is expected to vary locally and therefore implications of the strain rate assumption to the first stage ignition should be considered carefully in the future studies. In addition, the igniting part of the manifold depends on the applied chemical mechanism and the current joint PDF TCI model. Interestingly, in a recent RANS study of Spray A by Pei et al. [14], a similar flattened trend with respect to the IDT and injection pressure was obtained with the TPDF combustion model.

4.6. Observations of ignition kernels near FLOL

The simulations predict an increase in FLOL with an increasing injection pressure, which is consistent with the experimental

observations in Fig. 4b. In momentum driven jets and sprays, the FLOL has been proposed to result from an auto-ignition based flame stabilization mechanism which is modulated by the surrounding flow dynamics [12,20,85–87]. Earlier we noted that the simulated FLOL was overpredicted for the highest 150MPa case.

As indicated earlier in Section 4.4, the high-temperature diffusion flame extends more upstream from the sides of the spray flame, which can be seen from e.g. the hydroxyl field in Fig. 8. Therefore, it is interesting to investigate the differences between the present cases close to the FLOL. Figure 12 shows a focused view of the instantaneous temperature fields in that area for the 50 and 150 MPa cases. The snapshots indicate the formation of small igniting gas pockets (I) at early stages of the flame development. After ignition, the kernels expand and merge with the other kernels (II) and convect downstream finally merging with the main flame (III). Simultaneously new ignition kernels are forming in other parts of the domain. The high and low injection pressures differ, as can be seen by comparing the structures indicated by III and IV. For the 50 MPa case the merged kernels draw the main flame more upstream, decreasing the FLOL. In contrast, the merging ignition kernels with 150 MPa are not stable and the upstream flame front finally breaks down into small high temperature pockets (IV and V). Simultaneously new ignition pockets are forming upstream (VI), which will undergo a similar evolution process as the earlier kernels. Thus, the main flame remains farther downstream, compared with the experimental FLOL results. Higher injection pressure also poses increased velocity fluctuations near the experimental FLOL locations (not shown). Similar numerical findings on the formation of ignition kernels and their role in the flame stabilization in LES Spray A context were recently reported by Pei et al. [20].

Due to the connection between the location of the appearing ignition kernel and FLOL, the local mixing conditions and turbulence levels play a role in the correct FLOL estimation. Typically ignition and combustion occur only at locations where the fluctuations are low enough and where sufficient mixing has occurred. It seems that the current numerical model is unable to predict the appearance of ignition kernels upstream enough
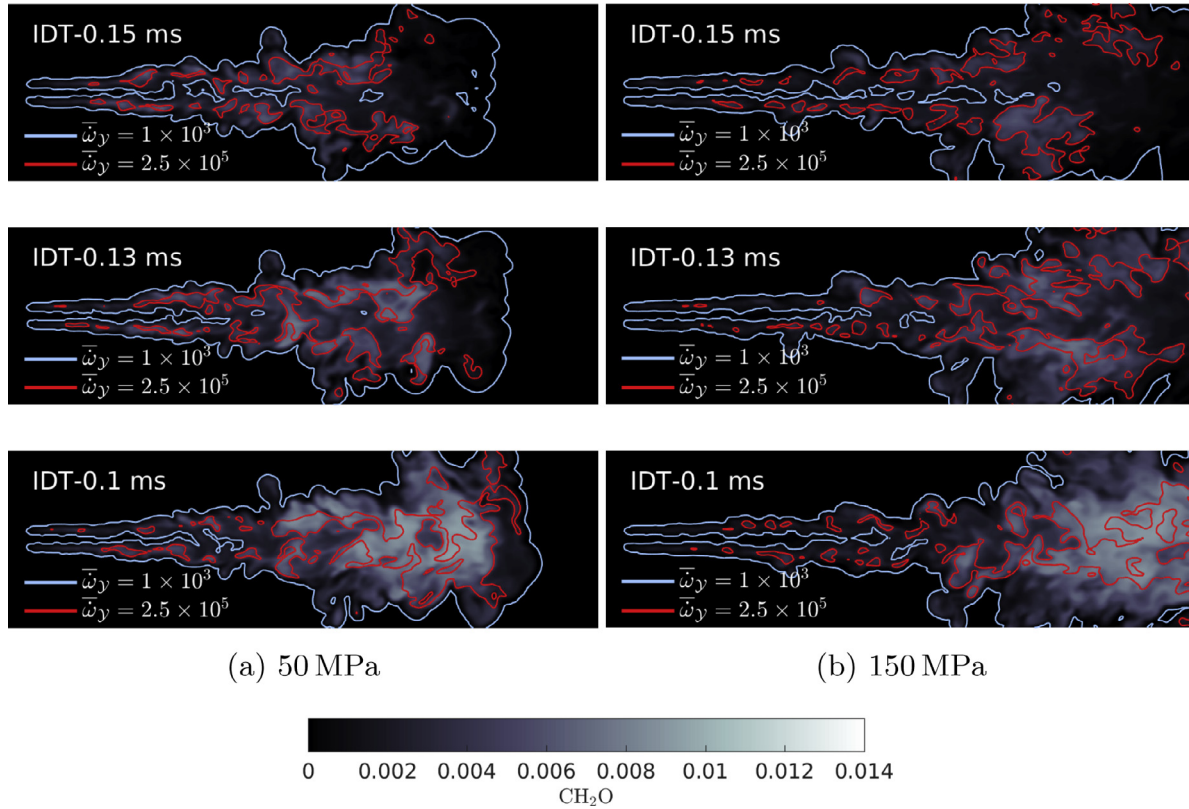
Fig. 11. Formaldehyde (CH_2O) field at $t = IDT - 0.15$ ms, $t = IDT - 0.13$ ms and at $t = IDT - 0.1$ ms for the (a) 50 MPa case and (b) 150 MPa cases. The light blue and red contour lines present the progress variable source term values $\overline{\dot{\omega}}_y = 1000 \, \text{kg m}^{-3}\text{s}^{-1}$ and $\overline{\dot{\omega}}_y = 2.5 \times 10^5 \, \text{kg m}^{-3}\text{s}^{-1}$, respectively. (For interpretation of the references to color in this figure legend, the reader is referred to the web version of this article).

for the 150 MPa case, leaving the main flame downstream from the experimental FLOL. It is worth noting that the presented results should be considered as features produced by the current LES-FGM model. In the present model, ignition of a gas pocket is governed by the single igniting flamelet with a specific strain rate. This simplification may influence the presented results and should be carefully considered in the future studies. However, the present results support the experimental observations, relating the FLOL and stable ignition kernel formation together [12,20,85–87]. Furthermore, we note, that since the LES based FLOL was determined by the azimuthally Favre-averaged OH threshold, the single kernel-wise high OH effects on FLOL are decreased.

### 4.7. Manifold landscape analysis based on mean axial flow

Next, we investigate the actual operation of the LES-FGM coupling with particular focus on fluid element combustion pathway along the spray axis. The following analysis shows differences in this coupling between different injection pressures, which can be linked to the overprediction of FLOL for the 150 MPa case as noted earlier in Fig. 4b.

Figure 13a shows how the time-averaged normalized progress variable $\mathcal{C}$ (see Eq. (12)) increases rather linearly along the spray axis before reaching the downstream high-temperature diffusion flame. However, a closer look at the 150 MPa case shows a somewhat flattened trend at 20mm, which is not observed for lower injection pressures. This indicates that reactions are slowing down, which is further investigated by considering the progress variable source term $\langle \dot{\omega}_y \rangle$.

As the source term describes the rate of change of $\mathcal{Y}$ (consequently $\mathcal{C}$) in the system and fluid dynamics time scales depend on the injection pressure, it is beneficial to relate the axial loca-

tion in space to time. In this kind of a system, transported particles could be used to link time, space and manifold variables with one-another. Here, we do not have such particles available but, instead, we attempt to link the spatial axial profiles, e.g. in Fig. 13a, to time. In brief, the procedure is as follows 1) construct the mean velocity profiles $\langle u(z) \rangle$ along the spray axis and 2) define a residence time by numerical integration: $t_{ax}^* = \int_0^{z_{ax}} dz / \langle u(z) \rangle$. In the above approach, we are envisioning that an average fluid element at point z_{ax} has spent an average residence time of t_{ax}^* in the system. Thus, t_{ax}^* enables correlating fluid parcel's relative axial location with time. Figure 13b shows the temporally averaged progress variable source term along the spray axis as a function of the defined residence time. It is evident that the observed bend in Fig. 13a is related to the decreased source term production after $t_{ax}^* = 0.07$ ms.

Possible explanations for the sudden decrease of $\langle \dot{\omega}_y \rangle$ are found by mapping the mean axial profiles of mixture fraction and progress variable onto the relevant FGM table. Such trajectories within the manifold are presented in Fig. 14, which shows the tabulated progress variable source term values as a function of $\mathcal{C}$ and Z. As TCI is employed herein, the actual tabulated value depends also on the value of mixture fraction variance Z''^2. Hence, representative values $Z''^2 = 1\text{e}{-}05$ and $Z''^2 = 5\text{e}{-}04$ are chosen for comparison. The trajectory starts from the fuel rich conditions with low chemical activity at the lower right corner, describing the conditions of a fluid element near the nozzle. Progressively the trajectory evolves towards leaner mixtures and chemically active regions farther downstream. The trajectories can be linked to the mean profiles in Fig. 13a and b by the colored markers, representing the current value of t_{ax}^*. It can be seen that the higher injection pressure spray reaches leaner conditions faster than the lower injection pressure and the local maximum of the progress variable source term is obtained near $t_{ax}^* = 0.08$ ms. However, the 150 MPa
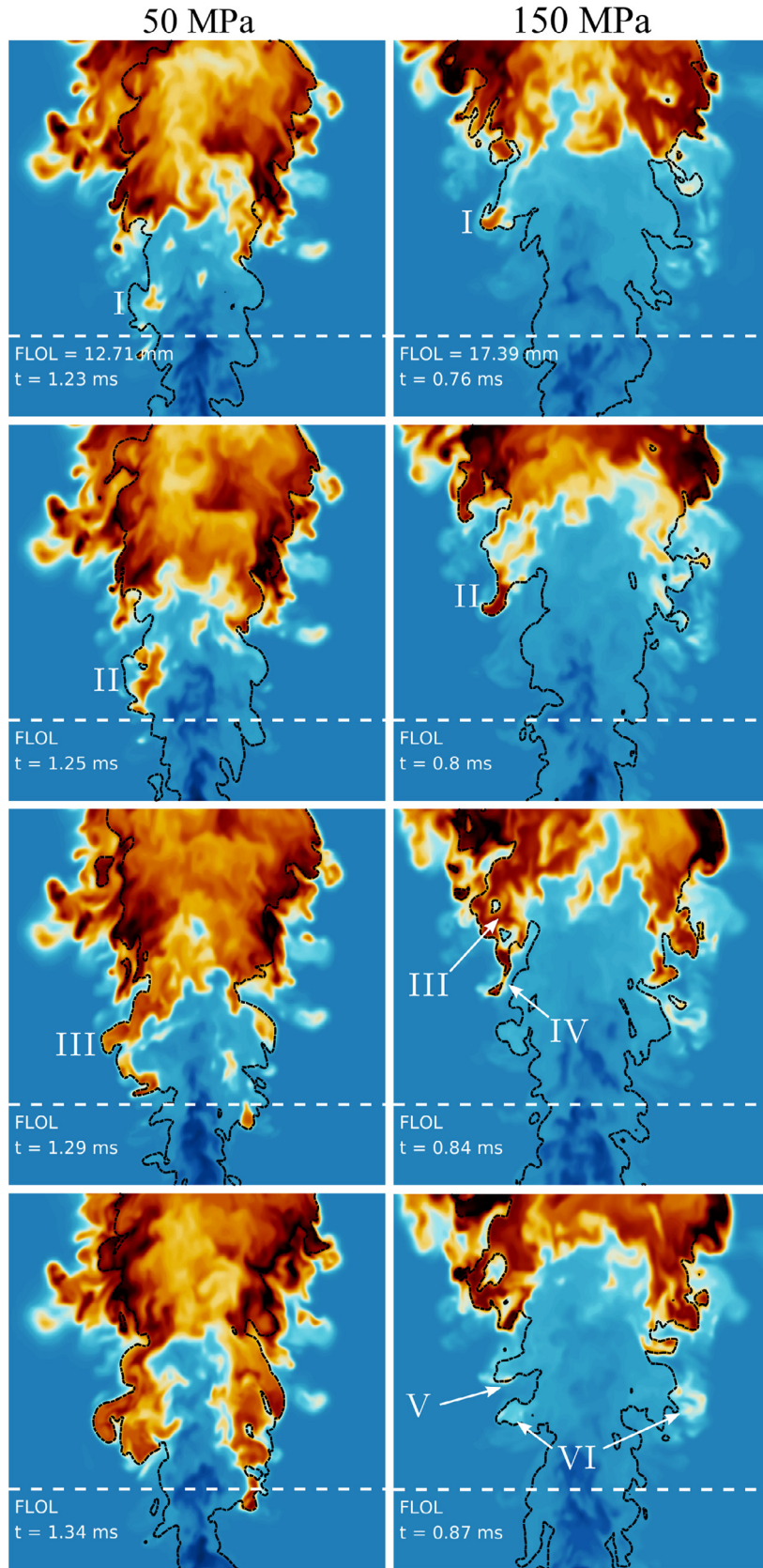
Fig. 12. Examples of time history of the temperature fields in the vicinity of the FLOL position. Left column: 50 MPa case, right column: 150 MPa case. White line represents the experimental FLOL [6] and the black dashed line represents the stoichiometric mixture fraction isoline. It should be noted that the plots are shifted in axial direction in order to align the FLOL.
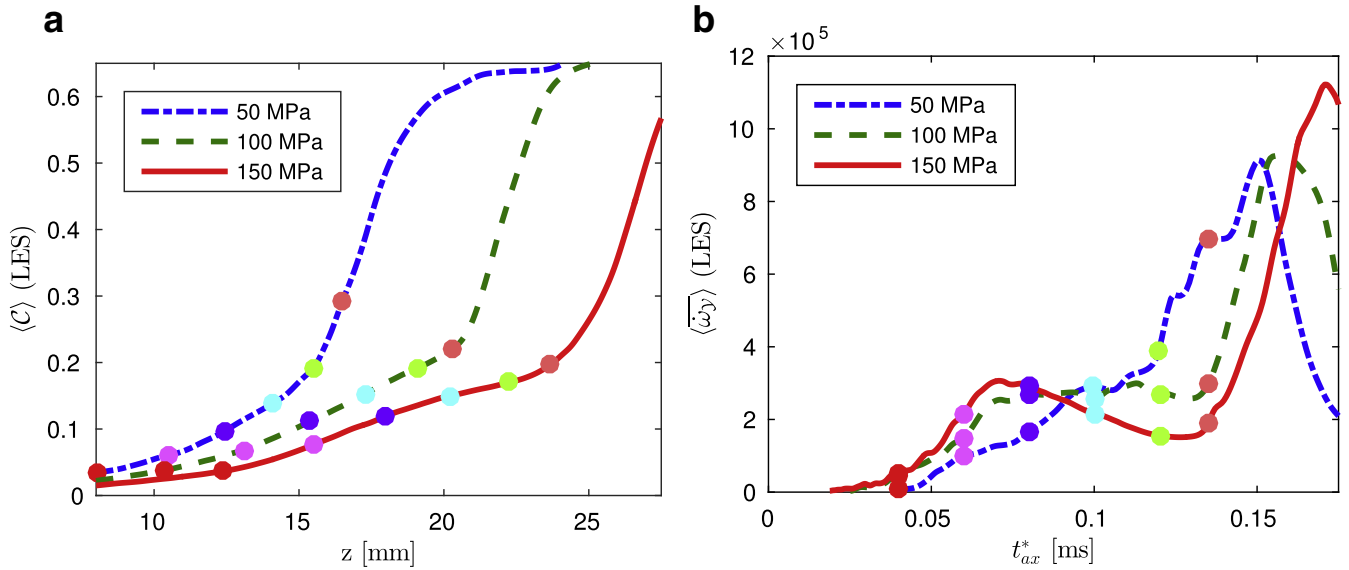
Fig. 13. (a) Temporally averaged axial profile of the normalized progress variable $\mathcal{C}$ as a function of axial location and (b) the corresponding progress variable source term $\langle \dot{\omega}_y \rangle$ as a function of residence time t^*_{ax}. The colored circles describe the instances in time: ● $t^*_{ax} = 0.04$, ● $t^*_{ax} = 0.06$, ● $t^*_{ax} = 0.08$, ● $t^*_{ax} = 0.1$, ● $t^*_{ax} = 0.12$ and ● $t^*_{ax} = 0.135$ ms. (For interpretation of the references to color in this figure legend, the reader is referred to the web version of this article).
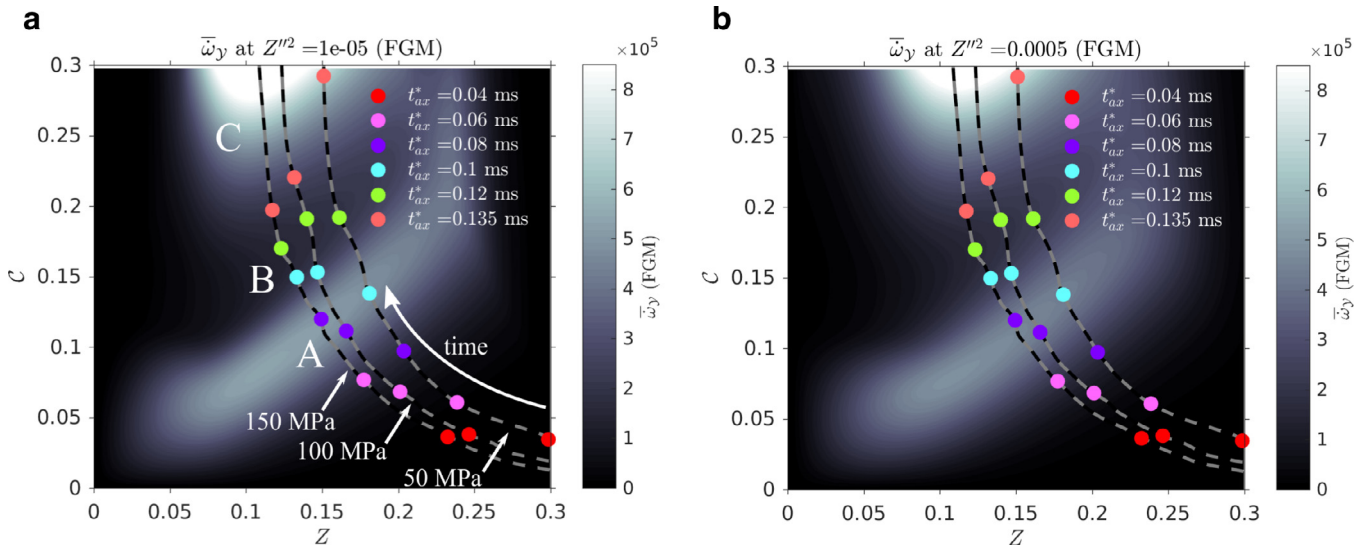
Fig. 14. The mean trajectory of a fluid element along the spray axis, superimposed onto the chemistry manifold with two mixture fraction variance values: (a) $Z''^2 = 1e{-}05$ and (b) $Z''^2 = 5e{-}04$. The colored circles describe the residence time instances: ● $t^*_{ax} = 0.04$, ● $t^*_{ax} = 0.06$, ● $t^*_{ax} = 0.08$, ● $t^*_{ax} = 0.1$, ● $t^*_{ax} = 0.12$ and ● $t^*_{ax} = 0.135$ ms. (For interpretation of the references to color in this figure legend, the reader is referred to the web version of this article).

case continues to promote stronger mixing and the trajectory of the average fluid element passes by the local maximum on the island (A) and falls into the valley (B), with lower source term values. The average fluid parcel of the high injection pressure case remains in the valley for a characteristic time, allowing moderate production of $\mathcal{C}$. Finally, the trajectories proceed towards the high source term values on the island (C), corresponding to the onset of the high-temperature diffusion flame. A different pathway is observed for the 50 MPa case. In general, the trajectory stays at richer conditions which at first retards the overall progress of reactions, but later on helps to avoid the valley (B), implying strongly monotonic progress in Fig. 13a.

Naturally, the mean flow analysis on the spray axis does not explain the progress of combustion in the periphery of the spray axis, which is important in terms of FLOL and local ignition kernel formation, discussed in the previous Section 4.6. Additionally, the mean flow based analysis does not account for turbulent

dispersion of fluid elements. However, the provided analysis can be useful in understanding the deviation in FLOL value for the 150 MPa case in terms of the manifold sensitivity. In particular, when considering the envisioned axial trajectories inside the manifold, the discrepancies in FLOL are expected to be similarly sensitive to 1) mixture formation and 2) to the manifold structure, which is a function of the underlying chemical model. The role of the algebraic TCI model is not extensively analyzed here, but we will assess the source term sensitivity to the manifold control variables, including the mixture fraction variance, in the next section.

4.8. Manifold sensitivity analysis

Above we discussed the trajectories of an average fluid element projected on representative $Z\mathcal{C}$-manifolds. According to Eq. (13), the mixture fraction variance influences the local source term values in the current TCI model, making the manifold and
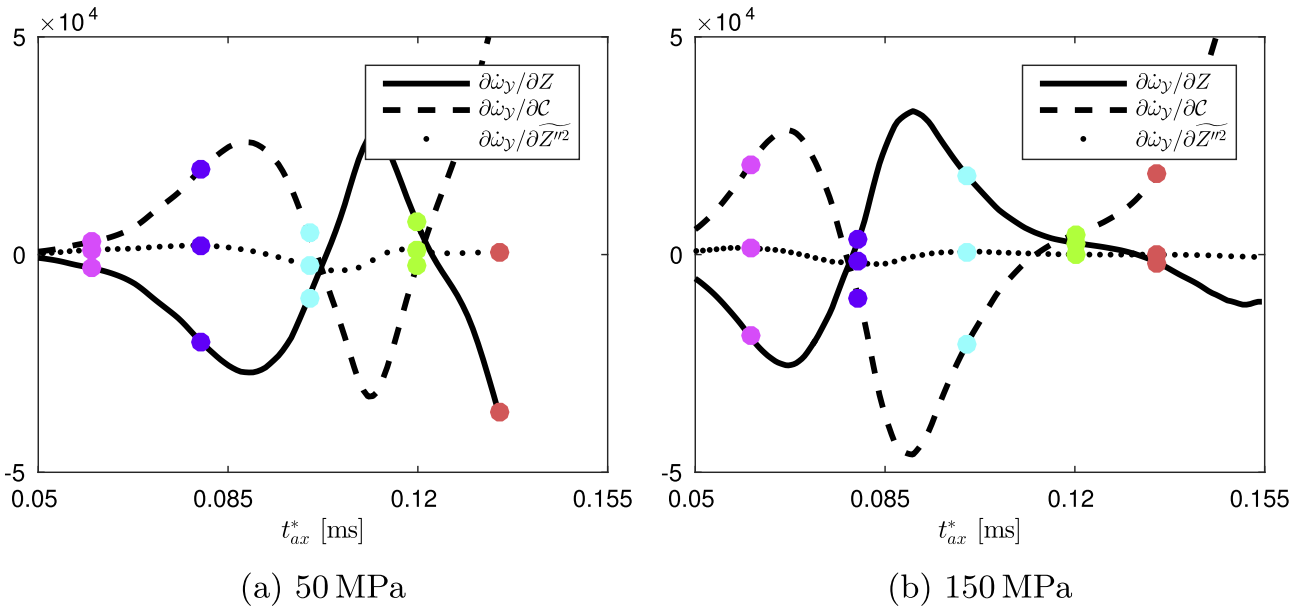
Fig. 15. Partial derivatives of progress variable source term with respect to the mixture fraction, progress variable and mixture fraction variance along the trajectories in Fig. 14. On the left (a) the 50 MPa case and on the right (b) the 150 MPa case. The colored circles describe the instances in time: ● $t^*_{ax} = 0.04$, ● $t^*_{ax} = 0.06$, ● $t^*_{ax} = 0.08$, ● $t^*_{ax} = 0.1$, ● $t^*_{ax} = 0.12$ and ● $t^*_{ax} = 0.135$ ms. (For interpretation of the references to color in this figure legend, the reader is referred to the web version of this article).

the prescribed trajectories in fact three-dimensional. In order to demonstrate the relatively weak TCI influence, Fig. 14 displays two different variance levels, representative to the present cases after the integrated time values $t^*_{ax} > 0.06$ ms. Higher variance smooths the underlying source term field but the implications of the previous analysis remain valid. To further explore the sensitivity of the progress variable source term along the trajectories in Fig. 14, the partial derivatives of the source term, $\partial\dot{\omega}_y/\partial Z$, $\partial\dot{\omega}_y/\partial\mathcal{Y}$ and $\partial\dot{\omega}_y/\partial Z''^2$ are plotted for the highest and lowest injection pressure cases in Fig. 15. It is evident that the highest sensitivity is shared among the mixture fraction and the progress variable, whereas the mixture fraction variance has the lowest sensitivity on the source term. The most distinctive difference between the two cases is that effectively, the fluid element of the higher injection pressure case spends more time in the low source term region (valley B, from purple marker to green marker), compared to the lower injection pressure case (from cyan marker to green marker).

Previously, in Fig. 2, we noted underpredicted values for the mixture fraction radial profiles around 20 mm axial locations for all cases. The above analysis indicates that this underprediction may influence the FLOL establishment. Enhanced mixing dilutes the vapor mixture to lower Z-values, further enabling an increased progress variable source term value. Yet, dilution may also retard the progress of combustion as shown in the analysis above. As Figs. 14 and 15 indicate, the analysis of an average fluid element trajectory in the FGM manifold is a descriptive way to understand the quasi-steady features such as the FLOL of diffusion flames.

5. Conclusions

A recently developed LES-FGM model has been utilized for the reacting ECN Spray A target conditions at three different injection pressures (50, 100 and 150 MPa). The first part of the paper was involved with validation of spray-submodels for the non-reacting sprays (objective 1). A relatively good agreement was obtained with respect to the liquid length and vapor penetrations whereas the average radial mixture fraction profiles were underestimated for all the three pressures.

The second objective was to carry out the reacting LES simulation and to provide quantitative comparison with the experimental data. Such a comparison was shown in Section 4.2 in terms of IDT, FLOL and chamber pressure rise. Additionally, qualitative comparison of spatial hydroxyl field to experimental PLIF images was carried out. Results showed a maximum deviation of 20% with respect to IDT of the 50 MPa case, whereas the agreement improved for the 150 MPa case. The FLOL was overestimated only slightly for the 50 MPa case but approximately 14% deviation was found for the 150 MPa case. The noted discrepancies were investigated by considering the evolution of the averaged FGM control variables, i.e. mixture fraction and progress variable, along the spray axis. In particular, the introduced FGM trajectory analysis of an average fluid element in a quasi-steady diffusion flame was found to be a simple and descriptive way in explaining possible reasons for the differences in experimentally and numerically observed FLOL values. Additionally, numerical examples showed a high sensitivity of the reaction progress to local mixture formation at axial locations near the FLOL, linking the uncertainties in mixture fraction radial profiles to the noted discrepancies in FLOL results, therefore fulfilling the fifth objective.

Concerning the fourth and fifth objectives, the combustion analysis was further enriched by a statistical analysis of resolved hydroxyl and formaldehyde distributions in ZT-plane. This showed how the onset of the first-stage ignition takes place close to the stoichiometric conditions, whereas the following chemical activity takes place at richer conditions. In addition, for the 50 MPa case, the formaldehyde generation is noted to be more concentrated to regions of rich mixture fractions, while OH being concentrated around the stoichiometric mixture areas. The length of the formaldehyde pool was also quantified. Igniting gas pockets (i.e. ignition kernels) could be observed near the FLOL and the numerical results support their role as an auto-ignition based flame stabilization mechanism, experimentally observed in [12,85,86]. A higher injection pressure was noted to suppress the ignition kernel evolution, also supporting experimental observations. The present LES-FGM approach can therefore be considered to capture various aspects of spray combustion physics as reported in literature (objective 3).

Acknowledgments

References

[1] R.D. Reitz, G. Duraisamy, Review of high efficiency and clean reactivity controlled compression ignition (RCCI) combustion in internal combustion engines, Prog. Energy Combust. Sci. 46 (2015) 12–71, doi:10.1016/j.pecs.2014.05.003.

[2] J.E. Dec, Advanced compression-ignition engines – understanding the in-cylinder processes, Proc. Combust. Inst. 32 II (2) (2009) 2727–2742, doi:10.1016/j.proci.2008.08.008.

[3] Home page: Engine Combustion Network (ECN): Experimental diagnostics and experimental data: URL: https://ecn.sandia.gov/diesel-spray-combustion/. (Accessed 16.01.2018).

[4] R. Payri, J.M. García-Oliver, M. Bardi, J. Manin, Fuel temperature influence on diesel sprays in inert and reacting conditions, Appl. Thermal Eng. 35 (1) (2012) 185–195, doi:10.1016/j.applthermaleng.2011.10.027.

[5] J. Benajes, R. Payri, M. Bardi, P. Martí-Aldaraví, Experimental characterization of diesel ignition and lift-off length using a single-hole ECN injector, Appl. Thermal Eng. 58 (1–2) (2013) 554–563, doi:10.1016/j.applthermaleng.2013.04.044.

[6] N. Maes, M. Meijer, N. Dam, B. Somers, H. Baya Toda, G. Bruneaux, S.A. Skeen, L.M. Pickett, J. Manin, Characterization of Spray A flame structure for parametric variations in ECN constant-volume vessels using chemiluminescence and laser-induced fluorescence, Combust. Flame 174 (2016) 138–151, doi:10.1016/j.combustflame.2016.09.005.

[7] M. Bardi, T. Bazyn, G. Bruneaux, J. Johnson, S.-Y. Lee, L.M. Malbec, M. Meijer, J. Naber, R. Payri, L.M. Pickett, B. Somers, Engine combustion network (Ecn): characterization and comparison of boundary conditions for different combustion vessels, At. Sprays 22 (9) (2012) 777–806, doi:10.1615/AtomizSpr.2012006083.

[8] M. Bardi, R. Payri, L.M. Malbec, G. Bruneaux, L.M. Pickett, J. Manin, T. Bazyn, C. Genzale, Engine combustion network: comparison of spray development, vaporization, and combustion in different combustion vessels, At. Sprays 22 (10) (2012) 807–842, doi:10.1615/AtomizSpr.2013005837.

[9] S.A. Skeen, J. Manin, L.M. Pickett, Simultaneous formaldehyde PLIF and high-speed schlieren imaging for ignition visualization in high-pressure spray flames, Proc. Combust. Inst. 35 (3) (2015) 3167–3174, doi:10.1016/j.proci.2014.06.040.

[10] D.L. Siebers, Liquid-phase fuel penetration in diesel sprays, in: SAE Technical Paper 980809, 1998. doi:10.4271/980809.

[11] L.M. Pickett, D.L. Siebers, Soot in diesel fuel jets: effects of ambient temperature, ambient density, and injection pressure, Combust. Flame 138 (1–2) (2004) 114–135, doi:10.1016/j.combustflame.2004.04.006.

[12] L.M. Pickett, D.L. Siebers, C.A. Idicheria, Relationship between ignition processes and the lift-off length of diesel fuel jets, in: SAE Technical Paper, 724, 2005, pp. –. doi:10.4271/2005-01-3843.

[13] S. Banerjee, C.J. Rutland, Study on spray induced turbulence using large eddy simulations, At. Sprays 25 (4) (2015) 285–316, doi:10.1615/AtomizSpr.2015006910.

[14] Y. Pei, E.R. Hawkes, S. Kook, G.M. Goldin, T. Lu, Modelling n-dodecane spray and combustion with the transported probability density function method, Combust. Flame 162 (5) (2015) 2006–2019, doi:10.1016/j.combustflame.2014.12.019.

[15] G. D'Errico, T. Lucchini, F. Contino, M. Jangi, X.-S. Bai, Comparison of well-mixed and multiple representative interactive flamelet approaches for diesel spray combustion modelling, Combust. Theory Model. 18 (1) (2014) 65–88, doi:10.1080/13647830.2013.860238.

[16] P. Kundu, Y. Pei, M. Wang, R. Mandhapati, S. Som, Evaluation of turbulence-chemistry interaction under diesel engine conditions with multi-flamelet rif model, At. Sprays 24 (9) (2014) 779–800, doi:10.1615/AtomizSpr.2014010506.

[17] S. Bhattacharjee, D.C. Haworth, Simulations of transient n-heptane and n-dodecane spray flames under engine-relevant conditions using a transported PDF method, Combust. Flame 160 (10) (2013) 2083–2102, doi:10.1016/j.combustflame.2013.05.003.

[18] C. Gong, M. Jangi, X.S. Bai, Large eddy simulation of n-dodecane spray combustion in a high pressure combustion vessel, Appl. Energy 136 (2014) 373–381, doi:10.1016/j.apenergy.2014.09.030.

[19] C. Gong, M. Jangi, T. Lucchini, G. D'Errico, X.S. Bai, Large eddy simulation of air entrainment and mixing in reacting and non-reacting diesel sprays, Flow Turbul. Combust. 93 (3) (2014) 385–404, doi:10.1007/s10494-014-9566-0.

[20] Y. Pei, S. Som, E. Pomraning, P.K. Senecal, S.A. Skeen, J. Manin, L.M. Pickett, Large eddy simulation of a reacting spray flame with multiple realizations under compression ignition engine conditions, Combust. Flame 162 (12) (2015) 4442–4455, doi:10.1016/j.combustflame.2015.08.010.

[21] C.K. Blomberg, L. Zeugin, S.S. Pandurangi, M. Bolla, K. Boulouchos, Y.M. Wright, Modeling split injections of ECN Spray A using a conditional moment closure combustion model with RANS and LES, SAE Int. J. Engines 9 (4) (2016) 2107–2119, doi:10.4271/2016-01-2237.

[22] L. Hakim, G. Lacaze, J. Oefelein, Large eddy simulation of autoignition transients in a model diesel injector configuration, SAE Int. J. Fuels Lubr. 9 (1) (2016) 165–176, doi:10.4271/2016-01-0872.

[23] F. Bottone, A. Kronenburg, D. Gosman, A. Marquis, The numerical simulation of diesel spray combustion with LES-CMC, Flow Turbul. Combust. 89 (4) (2012) 651–673, doi:10.1007/s10494-012-9415-y.

[24] Y. Pei, E.R. Hawkes, S. Kook, Transported probability density function modelling of the vapour phase of an n-heptane jet at diesel engine conditions, Proc. Combust. Inst. 34 (2) (2013) 3039–3047, doi:10.1016/j.proci.2012.07.033.

[25] F. Bouras, A. Soudani, M. Si-Ameur, Beta-PDF approach for large-eddy simulation of non-premixed turbulent combustion, Int. Rev. Mech. Eng. 4 (3) (2010) 358–363, doi:10.1017/S0022112004008213.

[26] N. Peters, A.M. Kanury, Turbulent combustion, Cambridge University Press, 2000, doi:10.1017/CBO9780511612701.

[27] M.M. Ameen, J. Abraham, RANS and LES study of lift-off physics in reacting diesel jets, in: SAE Technical Papers, volume 1, 2014. doi:10.4271/2014-01-1118.

[28] C. Bekdemir, L.M.T. Somers, L.P.H. De Goey, J. Tillou, C. Angelberger, Predicting diesel combustion characteristics with large-eddy simulations including tabulated chemical kinetics, Proc. Combust. Inst. 34 (2) (2013) 3067–3074, doi:10.1016/j.proci.2012.06.160.

[29] J. Tillou, J.-B. Michel, C. Angelberger, C. Bekdemir, D. Veynante, Large-eddy simulation of diesel spray combustion with exhaust gas recirculation, Oil Gas Sci. Technol. Revue d'IFP Energies nouvelles 69 (1) (2013) 155–165, doi:10.2516/ogst/2013139.

[30] A. Wehrfritz, O. Kaario, V. Vuorinen, B. Somers, Large eddy simulation of n-dodecane spray flames using flamelet generated manifolds, Combust. Flame 167 (2016) 113–131, doi:10.1016/j.combustflame.2016.02.019.

[31] E. Ranzi, A. Frassoldati, A. Stagni, M. Pelucchi, A. Cuoci, T. Faravelli, Reduced kinetic schemes of complex reaction systems: fossil and biomass-derived transportation fuels, Int. J. Chem. Kinet. 46 (9) (2014) 512–542, doi:10.1002/kin.20867.

[32] K. Narayanaswamy, P. Pepiot, H. Pitsch, A chemical mechanism for low to high temperature oxidation of n-dodecane as a component of transportation fuel surrogates, Combust. Flame 161 (4) (2014) 866–884, doi:10.1016/j.combustflame.2013.10.012.

[33] Z. Luo, S. Som, S.M. Sarathy, M. Plomer, W.J. Pitz, D.E. Longman, T. Lu, Development and validation of an n-dodecane skeletal mechanism forspray combustion applications, Combust. Theory Model. 18 (2) (2014) 187–203, doi:10.1080/13647830.2013.872807.

[34] S. Som, D.E. Longman, Z. Luo, M. Plomer, T. Lu, Longman, Luo, Plomer, Three dimensional simulations of diesel sprays using n-dodecane as a surrogate (Ci) (2011) 1–14.

[35] T. Yao, Y. Pei, B.-J. Zhong, S. Som, T. Lu, A hybrid mechanism for n-dodecane combustion with optimized low-temperature chemistry, 9th US National Combustion Meeting (2015), pp. 1–10.

[36] X. Jiang, G.A. Siamas, K. Jagus, T.G. Karayiannis, Physical modelling and advanced simulations of gas-liquid two-phase jet flows in atomization and sprays, Prog. Energy Combust. Sci. 36 (2) (2010) 131–167, doi:10.1016/j.pecs.2009.09.002.

[37] S. Subramaniam, Lagrangian–Eulerian methods for multiphase flows, Prog. Energy Combust. Sci. 39 (2–3) (2013) 215–245, doi:10.1016/j.pecs.2012.10.003.

[38] A. Irannejad, F. Jaberi, Numerical study of high speed evaporating sprays, Int. J. Multiph. Flow 70 (2015) 58–76, doi:10.1016/j.ijmultiphaseflow.2014.11.014.

[39] A. Irannejad, A. Banaeizadeh, F. Jaberi, Large eddy simulation of turbulent spray combustion, Combust. Flame 162 (2) (2015) 431–450, doi:10.1016/j.combustflame.2014.07.029.

[40] Q. Xue, S. Som, P.K. Senecal, E. Pomraning, Large eddy simulation of fuel spray under non-reacting IC engine conditions, At. Sprays 23 (x) (2013) 1–30, doi:10.1615/AtomizSpr.2013008320.

[41] H. Jasak, H.G. Weller, A.D. Gosman, High resolution NVD differencing scheme for arbitrarily unstructured meshes, Int. J. Numer. Methods Fluids 31 (2) (1999) 431–449, doi:10.1002/(SICI)1097-0363(19990930)31:2(431::AID-FLD884)3.0.CO;2-T.

[42] OpenFOAM Foundation – The Open Source Computational Fluid Dynamics (CFD) Toolbox. URL: https://openfoam.org/. Source code available at URL: https://github.com/OpenFOAM (Accessed 16.91.2018).

[43] T.-d. Homogeneous, Implicit large eddy simulation of, 131, Cambridge University Press, 2015, doi:10.1115/1.3077141.

[44] F.F. Grinstein, C. Fureby, On flux-limiting-based implicit large eddy simulation, J. Fluids Eng. 129 (12) (2007) 1483, doi:10.1115/1.2801684.

[45] A. Aspden, N. Nikiforakis, S. Dalziel, J. Bell, Analysis of implicit LES methods, Commun. Appl. Math. Comput. Sci. 3 (1) (2008) 103–126, doi:10.2140/camcos.2008.3.103.

[46] C. Fureby, F.F. Grinstein, Large eddy simulation of high-Reynolds-number free and wall-bounded flows, J. Comput. Phys. 181 (1) (2002) 68–97, doi:10.1006/jcph.2002.7119.

[47] C. Fureby, F. Grinstein, Monotonically integrated large eddy simulation of free shear flows, AIAA J. 37 (5) (1999) 544–556, doi:10.2514/3.14208.

[48] V. Vuorinen, J. Yu, S. Tirunagari, O. Kaario, M. Larmi, C. Duwig, B.J. Boersma, Large-eddy simulation of highly underexpanded transient gas jets, Phys. Fluids 25 (1) (2013) 016101, doi:10.1063/1.4772192.

[49] V. Vuorinen, A. Wehrfritz, C. Duwig, B.J. Boersma, Large-eddy simulation on the effect of injection pressure and density on fuel jet mixing in gas engines, Fuel 130 (2014) 241–250, doi:10.1016/j.fuel.2014.04.045.

[50] M. Berglund, C. Fureby, LES of supersonic combustion in a scramjet engine model, Proc. Combust. Inst. 31 II (2) (2007) 2497–2504, doi:10.1016/j.proci.2006.07.074.

[51] A. Wehrfritz, V. Vuorinen, O. Kaario, M. Larmi, Large eddy simulation of high-velocity fuel sprays: studying mesh resolution and breakup model effects for Spray A, At. Sprays 23 (5) (2013) 419–442, doi:10.1615/AtomizSpr.2013007342.

[52] R.D. Reitz, Modeling atomization processes in high-pressure vaporizing sprays, At. Sprays 3 (1987) 309–337.

[53] R.D. Reitz, J.C. Beale, Modeling spray atomization with the Kelvin–Helmholtz/Rayleigh–Taylor hybrid model, At. Sprays 9 (6) (1999) 623–650, doi:10.1615/AtomizSpr.v9.i6.40.

[54] N. Frossling, Uber die verdunstung fallender tropfen, Geophysics 12 (1938) 170–216.

[55] W.E. Ranz, W.R. Marshall, Evaporation from drops, part {I}, Chem. Eng. Prog. 48 (3) (1952) 173–180.

[56] W.E. Ranz, W.R. Marshall, Evaporation from drops, part {I}, Chem. Eng. Prog. 48 (3) (1952) 141–146.

[57] U. Maas, S.B. Pope, Simplifying chemical kinetics: intrinsic low-dimensional manifolds in composition space, Combust. Flame 88 (3–4) (1992) 239–264, doi:10.1016/0010-2180(92)90034-M.

[58] G. Dixon-Lewis, T. David, P.H. Gaskell, S. Fukutani, H. Jinno, J.A. Miller, R.J. Kee, M.D. Smooke, N. Peters, E. Effelsberg, J. Warnatz, F. Behrendt, Calculation of the structure and extinction limit of a methane-air counterflow diffusion flame in the forward stagnation region of a porous cylinder, Symp. (Int.) Combust. 20 (1) (1985) 1893–1904, doi:10.1016/S0082-0784(85)80688-3.

[59] L.P.H. De Goey, J.H.M. Ten Thije Boonkkamp, A mass-based definition of flame stretch for flames with finite thickness, Combust. Sci. Technol. 122 (1–6) (1997) 399–405, doi:10.1080/00102209708935618.

[60] G. Stahl, J. Warnatz, Numerical investigation of time-dependent properties and extinction of strained methane and propane-air flamelets, Combust. Flame 85 (3–4) (1991) 285–299, doi:10.1016/0010-2180(91)90134-W.

[61] Chem1D, A one-dimensional laminar flame code, Eindhoven University of Technology

[62] M. Ghaderi Masouleh, A. Wehrfritz, O. Kaario, H. Kahila, V. Vuorinen, Comparative study on chemical kinetic schemes for dual-fuel combustion of n-dodecane/methane blends, Fuel 191 (2017) 62–76, doi:10.1016/j.fuel.2016.10.114.

[63] J.C. Sutherland, P.J. Smith, J.H. Chen, Quantification of differential diffusion in nonpremixed systems, Combust. Theory Model. 9 (2) (2005) 365–383, doi:10.1080/17455030500150009.

[64] R.W. Bilger, S.H. Stårner, R.J. Kee, On reduced mechanisms for methane-air combustion in nonpremixed flames, Combust. Flame 80 (2) (1990) 135–149, doi:10.1016/0010-2180(90)90122-8.

[65] A.W. Cook, J.J. Riley, A subgrid model for equilibrium chemistry in turbulent flows, Phys. Fluids 6 (8) (1994) 2868, doi:10.1063/1.868111.

[66] C. Wall, B.J. Boersma, P. Moin, An evaluation of the assumed beta probability density function subgrid-scale model for large eddy simulation of non-premixed, turbulent combustion with heat release, Phys. Fluids 12 (10) (2000) 2522–2529, doi:10.1063/1.1287911.

[67] J. Janicka, W. Kollmann, A two-variables formalism for the treatment of chemical reactions in turbulent H_2–air diffusion flames, Symp. (Int.) Combust. 17 (1) (1979) 421–430, doi:10.1016/S0082-0784(79)80043-0.

[68] L. Vervisch, R. Hauguel, P. Domingo, M. Rullaud, Three facets of turbulent combustion modelling: DNS of premixed V-flame, LES of lifted nonpremixed flame and RANS of jet-flame, 2004, doi:10.1088/1468-5248/5/1/004.

[69] G.M. Goldin, S. Menon, A comparison of scalar PDF turbulent combustion models, Combust. Flame 113 (3) (1998) 442–453, doi:10.1016/S0010-2180(97)00237-X.

[70] C.D. Pierce, P. Moin, A dynamic model for subgrid-scale variance and dissipation rate of a conserved scalar, Phys. Fluids 10 (12) (1998) 3041–3044, doi:10.1063/1.869832.

[71] G. Balarac, H. Pitsch, V. Raman, Development of a dynamic model for the sub-filter scalar variance using the concept of optimal estimators, Phys. Fluids 20 (3) (2008) 035114, doi:10.1063/1.2896287.

[72] Universitat Politecnica de Valencia CMT Virtual Injection Rate Generator: Available online at URL http://www.cmt.upv.es/ECN03.aspx#model (Accessed 16.01.2018).

[73] L.M. Pickett, J. Manin, C.L. Genzale, D.L. Siebers, M.P.B. Musculus, C.A. Idicheria, Relationship between diesel fuel spray vapor penetration/dispersion and local fuel mixture fraction, SAE Int. J. Engines 4 (1) (2011) 764–799, doi:10.4271/2011-01-0686.

[74] J. Sato, K. Konishi, H. Okada, T. Niioka, Ignition process of fuel spray injected into high pressure high temperature atmosphere, Symp. (Int.) Combust. 21 (1) (1988) 695–702, doi:10.1016/S0082-0784(88)80301-1.

[75] C.F. Edwards, D.L. Siebers, D.H. Hoskin, Study of the autoignition process of a diesel spray via high speed visualization, in: SAE Technical Paper Series, 1992, pp. 1–18. doi:10.4271/920108.

[76] G. Bruneaux, Combustion structure of free and wall-impinging diesel jets by simultaneous laser-induced fluorescence of formaldehyde, poly-aromatic hydrocarbons, and hydroxides, Int. J. Engine Res. 9 (3) (2008) 249–265, doi:10.1243/14680874JER00108.

[77] C.A.J. Leermakers, M.P.B. Musculus, In-cylinder soot precursor growth in a low-temperature combustion diesel engine: laser-induced fluorescence of poly-cyclic aromatic hydrocarbons, Proc. Combust. Inst. 35 (3) (2015) 3079–3086, doi:10.1016/j.proci.2014.06.101.

[78] E. Mastorakos, Ignition of turbulent non-premixed flames, Prog. Energy Combust. Sci. 35 (1) (2009) 57–97, doi:10.1016/j.pecs.2008.07.002.

[79] R.N. Dahms, G.A. Paczko, S.A. Skeen, L.M. Pickett, Understanding the ignition mechanism of high-pressure spray flames, Proc. Combust. Inst. (2) (2016). https://doi.org/10.1016/j.proci.2016.08.023.

[80] Y. Pei, E.R. Hawkes, S. Kook, G.M. Goldin, Y. Yang, S.B. Pope, S. Som, An analysis of the structure of an n-dodecane spray flame using TPDF modelling, Combust. Flame 168 (2016) 420–435, doi:10.1016/j.combustflame.2015.11.034.

[81] P. Kundu, M.M. Ameen, S. Som, Importance of turbulence-chemistry interactions at low temperature engine conditions, Combust. Flame 183 (2017) 283–298, doi:10.1016/j.combustflame.2017.05.025.

[82] A. Krisman, E.R. Hawkes, M. Talei, A. Bhagatwala, J.H. Chen, Characterisation of two-stage ignition in diesel engine-relevant thermochemical conditions using direct numerical simulation, Combust. Flame 172 (2016) 326–341, doi:10.1016/j.combustflame.2016.06.010.

[83] A. Krisman, E.R. Hawkes, M. Talei, A. Bhagatwala, J.H. Chen, A direct numerical simulation of cool-flame affected autoignition in diesel engine-relevant conditions, Proc. Combust. Inst. 36 (3) (2017) 3567–3575, doi:10.1016/j.proci.2016.08.043.

[84] G. Borghesi, E. Mastorakos, R.S. Cant, Complex chemistry DNS of n-heptane spray autoignition at high pressure and intermediate temperature conditions, Combust. Flame 160 (2013) 1254–1275, doi:10.1016/j.combustflame.2013.02.009.

[85] E. Oldenhof, M.J. Tummers, E.H. van Veen, D.J.E.M. Roekaerts, Ignition kernel formation and lift-off behaviour of jet-in-hot-coflow flames, Combust. Flame 157 (6) (2010) 1167–1178, doi:10.1016/j.combustflame.2010.01.002.

[86] E. Oldenhof, M.J. Tummers, E.H. van Veen, D.J.E.M. Roekaerts, Role of entrainment in the stabilisation of jet-in-hot-coflow flames, Combust. Flame 158 (8) (2011) 1553–1563, doi:10.1016/j.combustflame.2010.12.018.

[87] L.M. Pickett, S. Kook, H. Persson, i. Andersson, Diesel fuel jet lift-off stabilization in the presence of laser-induced plasma ignition, Proc. Combust. Inst. 32 II (2) (2009) 2793–2800, doi:10.1016/j.proci.2008.06.082.